Regorda, A., Thieulot, C., van Zelst, I., Erdos, Z., Maia, J., Buiter, S. (2023): Rifting Venus: Insights From Numerical Modeling. - Journal of Geophysical Research: Planets, 128, 3, e2022JE007588.

https://doi.org/10.1029/2022JE007588

JGR Planets

RESEARCH ARTICLE
10.1029/2022JE007588

Key Points:

- A strong crustal diabase rheology is required to localize strain and develop rifts in our models
- A thin crust produces the melt required to support the hypothesis of Venus being currently volcanically active
- Crustal thicknesses of 25 and 35 km result in surface topographies comparable with rift topography observations of Venus

Supporting Information:

Supporting Information may be found in the online version of this article.

Correspondence to:

A. Regorda,
alessandro.regorda@protonmail.ch

Citation:

Regorda, A., Thieulot, C., van Zelst, I., Erdős, Z., Maia, J., & Buiter, S. (2023). Rifting Venus: Insights from numerical modeling. *Journal of Geophysical Research: Planets*, *128*, e2022JE007588. https://doi.org/10.1029/2022JE007588

Received 30 SEP 2022
Accepted 28 FEB 2023

Author Contributions:

Conceptualization: Alessandro Regorda, Cedric Thieulot, Iris van Zelst, Zoltán Erdős, Julia Maia, Susanne Buiter
Formal analysis: Alessandro Regorda
Investigation: Alessandro Regorda
Methodology: Alessandro Regorda, Cedric Thieulot, Iris van Zelst, Zoltán Erdős, Susanne Buiter
Software: Alessandro Regorda, Cedric Thieulot
Validation: Alessandro Regorda, Cedric Thieulot
Visualization: Alessandro Regorda, Iris van Zelst, Zoltán Erdős, Julia Maia, Susanne Buiter
Writing – original draft: Alessandro Regorda, Cedric Thieulot, Iris van Zelst, Zoltán Erdős, Julia Maia, Susanne Buiter
Writing – review & editing: Alessandro Regorda, Cedric Thieulot, Iris van Zelst, Zoltán Erdős, Julia Maia, Susanne Buiter

Rifting Venus: Insights From Numerical Modeling

Alessandro Regorda[1], Cedric Thieulot[2], Iris van Zelst[3], Zoltán Erdős[4,5], Julia Maia[6], and Susanne Buiter[4,5]

[1]Department of Earth Sciences, Università degli Studi di Milano, Milan, Italy, [2]Department of Earth Sciences, Utrecht University, Utrecht, The Netherlands, [3]Institute of Planetary Research, German Aerospace Center (DLR), Berlin, Germany, [4]The Helmholtz Centre Potsdam - GFZ German Research Centre for Geosciences, Potsdam, Germany, [5]Tectonics and Geodynamics, RWTH Aachen University, Aachen, Germany, [6]Observatoire de la Côte d'Azur, Laboratoire Lagrange, CNRS, Université Côte d'Azur, Nice, France

Abstract

Venus is a terrestrial planet with dimensions similar to the Earth, but a vastly different geodynamic evolution, with recent studies debating the occurrence and extent of tectonic-like processes happening on the planet. The precious direct data that we have for Venus is very little, and there are only few numerical modeling studies concerning lithospheric-scale processes. However, the use of numerical models has proven crucial for our understanding of large-scale geodynamic processes of the Earth. Therefore, here we adapt 2D thermomechanical numerical models of rifting on Earth to Venus to study how the observed rifting structures on the Venusian surface could have been formed. More specifically, we aim to investigate how rifting evolves under the Venusian surface conditions and the proposed lithospheric structure. Our results show that a strong crustal rheology such as diabase is needed to localize strain and to develop a rift under the high surface temperature and pressure of Venus. The evolution of the rift formation is predominantly controlled by the crustal thickness, with a 25 km-thick diabase crust required to produce mantle upwelling and melting. The surface topography produced by our models fits well with the topography profiles of the Ganis and Devana Chasmata for different crustal thicknesses. We therefore speculate that the difference in these rift features on Venus could be due to different crustal thicknesses. Based on the estimated heat flux of Venus, our models indicate that a crust with a global average lower than 35 km is the most likely crustal thickness on Venus.

Plain Language Summary

Venus is a planet that is roughly the same size as the Earth, and recent studies have debated the style of Venusian tectonics and how it differs from Earth. One such tectonic process is known as "rifting," where a tectonic plate gets extended and forms structures as in East Africa on Earth. These rift structures have been observed on Venus as well, but it is unclear how they formed under Venus' high surface temperature and pressure. Computer simulations have improved our understanding of the rifting process on Earth, so here we apply them to Venus to discover how rifting processes work under Venusian conditions. Our results show that the crust needs to consist of strong rocks in order for rifting to take place under Venus' conditions. The thickness of the crust also has a direct effect on the evolution of the rift and a thin crust favors the production of magma on Venus. We compare the surface topography of the rifts in our simulations with rift topographies observed on Venus. We find that different crustal thicknesses fit different rift observations on Venus. Therefore, we speculate that differences in rifts on Venus could be related to differences in the crustal thickness.

1. Introduction

Venus is often regarded as Earth's sister planet that holds the key to understanding the Earth and terrestrial planets (Wilson et al., 2021). Indeed, Venus' mass and radius are similar to those of Earth's, yet the evolution of the planet resulted in a hell-like environment of high surface temperatures (464°C) and pressures (9.3 MPa compared to Earth's surface pressure of 0.1 MPa) with clouds of sulfuric acid compared to the temperate life-sustaining environment on Earth. Hence, studying the difference in evolution and processes between the two planets could give us additional insights into the Earth.

Besides the differing surface conditions, another main difference between Earth and Venus is that Earth currently hosts plate tectonics, whereas on Venus we do not currently observe plate tectonics as we know it. This difference could stem from Venus' lack of surface water, which is generally assumed to be an important factor in driving Earth's plate tectonics, and the hypothesis that Venus is currently a dry planet based on water content observations

mostly limited to the atmosphere (Elkins-Tanton et al., 2007; Huang et al., 2013; Smrekar, Elkins-Tanton et al., 2007). However, there are indications that Venus might have experienced, or indeed still does experience, some other form of tectonics. Synthetic aperture radar data from the Magellan mission provided 98% imaging coverage of the planet, unveiling a large diversity of tectonic features (Saunders & Pettengill, 1991). However, the spatial resolution of this data is quite limited. The radar images have a spatial resolution in the order of 100 m (Saunders & Pettengill, 1991), while the altimetry-derived topography has a vertical resolution of roughly 80 m and horizontal resolution of 10 km (Ford & Pettengill, 1992). This lack of detailed data means that the ages and origins of Venus' geologic features are largely unknown.

Although limited, the available data sets of Venus allowed for almost global geologic mapping of Venus' surface (e.g., Ivanov & Head, 2011), which has lead to studies of the planet's lithosphere and potential current tectonic activity. Analyzing the surface images and topography, Sandwell and Schubert (1992) have found evidence for lithospheric subduction on large Venus coronae. Further on, Schubert and Sandwell (1995) identified approximately 10,000 km of potential subduction troughs based on observed morphological similarities to subduction troughs on Earth. The interpretation of subduction at coronae was further supported by experiments by Davaille et al. (2017). In addition, regional-scale geodynamic modeling showed that coronae could be formed via subduction caused by plume impingement of the lithosphere (Gerya, 2014), which could still be an ongoing process today (Gülcher et al., 2020). In line with that, recent volcanism on Venus has been suggested by several studies because of observed fluctuations in sulfur dioxide in the atmosphere of Venus (Esposito, 1984; Esposito et al., 1988) that could be caused by volcanic eruptions. Indeed, specific regions such as the Atla Regio have been recognized as potential sites of current tectonic and volcanic activity (Brossier et al., 2022; Shalygin et al., 2015).

To explain the observed surface features in a global dynamical context, theoretical and modeling studies of Venus have proposed various possible geodynamic regimes (e.g., Rolf et al., 2022), including the plutonic-squishy lid tectonic regime (Lourenço et al., 2020), delamination tectonics (Adams et al., 2022), subcrustal lid rejuvenation (Ghail, 2015), the episodic lid regime (Rolf, Steinberger, et al., 2018; Turcotte, 1993; Uppalapati et al., 2020), heat-pipe volcanism (Moore et al., 2017), and the movement of fragmented lithosphere similar to the deformation of the interior of continents of Earth (Byrne et al., 2021).

On a regional scale, there are widespread observations of rifts on Venus (in black Figure 1a), called “chasma” (plural “chasmata”), from radar-image interpretation of normal-fault-bounded graben structures (Harris & Bédard, 2015). In total, rifts on Venus have an estimated length of up to 40,000 km (Masursky et al., 1980; McGill et al., 1981; Schaber, 1982) covering approximately 36.5×10^6 km^2, or 7.9% of Venus' surface (Price & Suppe, 1995). Despite being a prominent feature on its surface, little is known about the mechanisms responsible for creating rifts on Venus beyond the assumption that they are extensional features (Magee & Head, 1995). This lack of knowledge stems from the large-scale uncertainties on Venus' first-order tectonic regime and the many unknowns regarding the rifting structures on Venus. For example, the absolute age of the rift features and their extension rate and relationship with other structural features, such as coronae, are largely unconstrained. Yet, the global geological mapping by Ivanov and Head (2011) has shown that these major rifts zones are stratigraphically among the youngest formations on the planet. In addition, Grimm (1994b) estimated that the recent surface strain rate of Venus should be around 10^{-17}–10^{-18} s^{-1} by the evaluation of the postimpact degradation of craters.

To provide some insights into the potential extension rates of rift systems and their formation, early modeling studies have attempted to model the topographic signature of rifts on Venus through lithospheric stretching models (Solomon & Head, 1984, 1985) as well as theoretical (Banerdt & Golombek, 1988) and simple extensional models (Smrekar, Hoogenboom, et al., 2007). However, to date the physical driving mechanism behind the observed rift surface expressions in an environment of high surface temperature and pressure remains elusive with no comprehensive modeling study into the dynamics of rifting on Venus yet attempted.

In contrast, rifting on Earth in both continental and oceanic settings has been extensively studied through modeling (e.g., Bollino et al., 2022; Brune & Autin, 2013; Erdős et al., 2014; Sim et al., 2020; Theunissen & Huismans, 2019; Theunissen et al., 2022) and observational studies (e.g., Nonn et al., 2019; Peron-Pinvidic et al., 2022; Tavani & Muñoz, 2012; Zwaan et al., 2020) alike. Modeling studies in particular have focused on different aspects of rifting, including the drivers behind large-scale rift deformation and geometry (e.g., Naliboff & Buiter, 2015; Petersen et al., 2018; Tetreault & Buiter, 2018), the accompanying surface expressions (e.g., Balázs et al., 2021; Beucher & Huismans, 2020; Neuharth et al., 2022; Sternai, 2020), and emerging fault patterns (e.g., Richter et al., 2021; Sharples et al., 2015; Theunissen & Huismans, 2022). These studies have lead to key

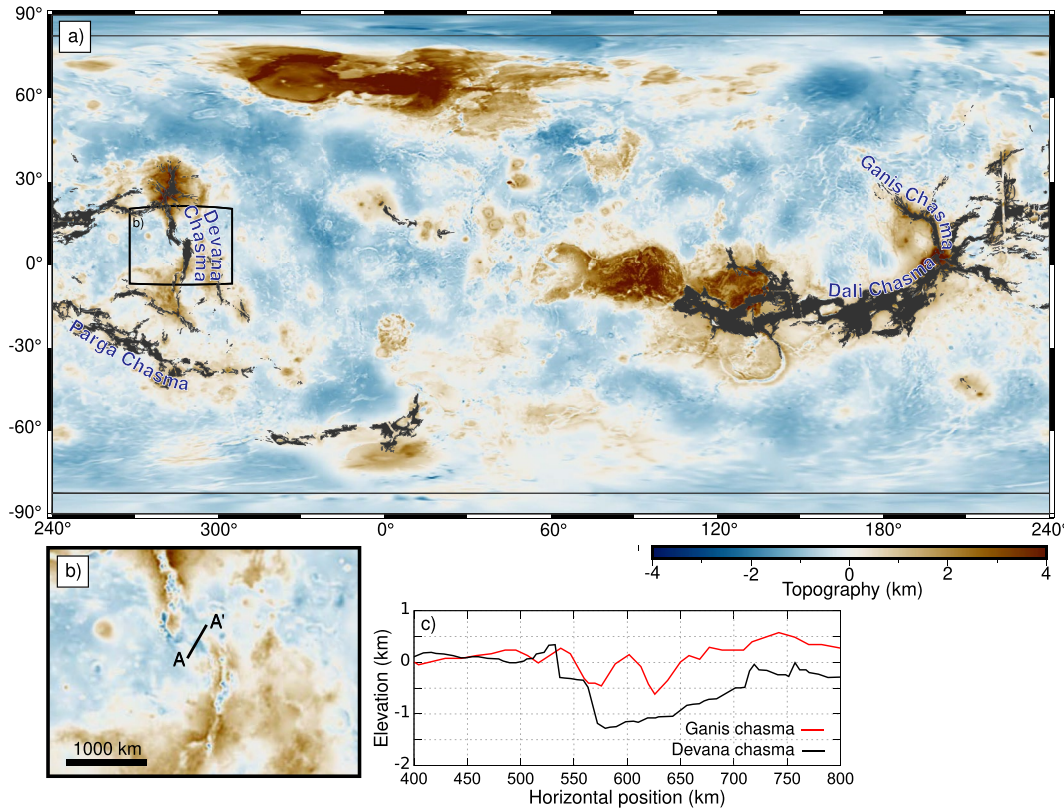

Figure 1. (a) Topographic map of Venus with the distribution of rift zones indicated in black (obtained from Ivanov and Head (2011)). (b) Zoom on Devana Chasma with the location of the topographic profile indicated. Both maps are in simple cylindrical projection. (c) Topographic profiles of Ganis Chasma (average) and Devana Chasma (along profile A-A′ in panel b).

insights into and a greater understanding of the rifting process on Earth. In particular, the key role of weakness zones, such as inherited structures and lithospheric heterogeneity, has been widely recognized for the localization of the strain and the development of tectonic structures in a divergent tectonic setting (e.g., Le Pourhiet et al., 2004; Wenker & Beaumont, 2018; van den Broek et al., 2020). Given the complexity of the settings in which continental rifting can initiate, many authors have studied the factors that can affect the evolution of continental rifting, such as the lithospheric strength (e.g., Andrés-Martínez et al., 2019; Dias et al., 2015; Jourdon et al., 2020; Liao et al., 2013), kinematic boundary conditions (e.g., Duretz et al., 2021; Korchinski et al., 2021; Püthe & Gerya, 2014; Zwaan et al., 2016), strain weakening (e.g., Allken et al., 2011; Choi et al., 2013; Huismans & Beaumont, 2003; Lavier et al., 1999, 2000), and temperature (e.g., Beniest et al., 2017; Manatschal et al., 2015; Petersen et al., 2015).

Considering the extensive modeling of rifting on Earth, a big outstanding question from a physical perspective is how modeling rifting on Venus would work with the increased surface temperature and pressure with respect to Earth. In other words, when considering Venusian surface conditions, are the ingredients typically used in the modeling of terrestrial rifts sufficient to create deformation in Venus' lithosphere? Previous studies (e.g., Foster & Nimmo, 1996) pointed out that brittle deformation would not occur on Venus in case of classical terrestrial rheology because of the high surface temperatures and pressures (e.g., Byrne et al., 2021; Gudkova & Zharkov, 2020; Gülcher et al., 2020). However, extensive surface faulting is observed on Venus and, therefore, the Venusian crust should be characterized by a stronger basaltic rheology, such as a diabase (Foster & Nimmo, 1996; Mackwell et al., 1998). In addition, the absence of water on Venus further increase the lithospheric strength (Foster & Nimmo, 1996). In fact, many authors have observed the similarities and differences between the rift features on Earth and Venus (e.g., Kiefer & Swafford, 2006; Solomon, 1993; Stoddard & Jurdy, 2012) and the rifts on Venus have been likened to continental rifts on Earth such as the East African rift (Basilevsky & McGill, 2007; Foster & Nimmo, 1996) and the Atlantic rift system prior to ocean opening (Graff et al., 2018). Rifts on Venus

are typically wider than their terrestrial equivalent, potentially due to a strong viscous surface layer (Zuber & Parmentier, 1986) or the lack of sediment infill (Foster & Nimmo, 1996). Uncertainties about Venus' crust also include both its composition, with a direct impact on the rheology, and its thickness. James et al. (2013) and Jiménez-Díaz et al. (2015) estimate that the average crustal thickness of Venus should be between 8 and 40 km. Localized gravity and topography studies showed that plateau highlands have crustal thicknesses of about 30 km and suggest that the average crustal thickness of Venus should be between 15 and 25 km (Grimm, 1994a; Maia & Wieczorek, 2022; Simons et al., 1997).

The observables for Venus to which we can compare are significantly more scarce than on Earth, but the topographic data provides profiles of rifts on Venus (e.g., Guseva, 2016; Guseva & Ivanov, 2019; Kiefer & Swafford, 2004; Stoddard & Jurdy, 2012) and modeling studies have provided various estimates of the global heat flow (Borrelli et al., 2021; Ghail, 2015; O'Rourke & Smrekar, 2018; Smrekar et al., 2022; Solomon et al., 1992). In addition, missions like EnVision (de Oliveira et al., 2018; Ghail et al., 2016) and VERITAS (Smrekar et al., 2020) are anticipated to provide a wealth of new information on Venus' surface and interior in the coming decade. Therefore, we believe it is time that a rift-modeling study like the ones so often used for Earth is applied to Venus to test how rifting takes place under the Venusian surface conditions.

Here, we use state-of-the-art numerical models of rifting on Earth and systematically change the model setup to reflect the conditions on Venus to assess how the rifting process works there and which numerical ingredients are needed to successfully model rifting on Venus. In particular, our goals are as follows:

1. Evaluate the impact of the surface temperature, pressure, and gravity of Venus on the lithospheric rheological behavior in a diverging tectonic setting and their consequences on localization and accumulation of strain and, ultimately, on the development of a continental rift.
2. Determine the effects of (a) strong crustal and mantle rheologies, such as diabase and dry dunite; (b) different types of weak seed; and (c) different crustal thicknesses on the evolution of a continental rift under Venusian conditions.
3. Compare the results of our Venusian models with the observed topography of two rift zones on Venus and estimates of Venus' surface flux from other modeling studies. This will allow us to assess whether different lithospheric thicknesses could be responsible for distinct structures on surface.

In the following, we first describe the employed numerical code and model setup (Section 2). We then describe the results obtained when changing the temperature, pressure, gravity, and rheology to Venus-like conditions, as well as different types of weak seeds and crustal thicknesses (Section 3). Last, we discuss how each change affects the rift formation and how well our models reproduce observed rift patterns on Venus (Section 4).

2. Methods

The numerical code that we have used in this work, coined FALCON (Finite element ALgorithm for COmputational aNalysis), is briefly described in the following section, while a complete description is presented in Regorda (2022). All the numerical methods described below have been thoroughly benchmarked with community benchmarks and, when available, analytical solutions. These passed benchmarks, as well as the features they test, are listed in Table 1; their descriptions and results can be found in Regorda (2022).

2.1. Numerical Methods

Flow is assumed to be incompressible and the extended Boussinesq approximation (e.g., Christensen & Yuen, 1985; Gassmöller et al., 2020) is used so that the mass, momentum, and energy conservation equations are as follows:

$$\vec{\nabla} \cdot \boldsymbol{\sigma} + \rho \vec{g} = \vec{0} \tag{1}$$

$$\vec{\nabla} \cdot \vec{u} = 0 \tag{2}$$

$$\rho_0 C_p \left(\frac{\partial T}{\partial t} + \vec{u} \cdot \vec{\nabla} T \right) = \vec{\nabla} \cdot \left(k \vec{\nabla} T \right) + \rho H + 2\eta \dot{\varepsilon}(\vec{u}) : \dot{\varepsilon}(\vec{u}) - \alpha T \rho \vec{g} u_y \tag{3}$$

Table 1
List of Benchmarks Passed to Test All the Feature Implemented in the FALCON Code

Feature tested	Benchmark	Reference
Stokes solver	Manufactured solution	Donea and Huerta (2003)
Markers advection	Zalesak disk	Zalesak (1979)
	Conservative Velocity Interpolation	Comparison with other codes
Momentum equation	Poiseuille flow	Thieulot (2014)
	Instantaneous 2D sphere	Comparison with other codes
	Rayleigh-Taylor experiment	Van Keken et al. (1997)
	Falling block	Gerya and Yuen (2003), Gerya (2010), and Thieulot (2011)
Sticky air and free surface	2D Stokes sphere	Comparison with other codes
	Stabilization algorithm	Kaus et al. (2010) and Thieulot (2014)
	Topography relaxation	Crameri et al. (2012)
	Spontaneous subduction	Schmeling et al. (2008)
Nonlinear rheology	Slab detachment	Schmalholz (2011) and Glerum et al. (2018)
	Indenter	Thieulot et al. (2008), Thieulot (2014), and Glerum et al. (2018)
	Brick	Glerum et al. (2018)
Energy equation	Advection stabilization	Donea and Huerta (2003) and Thieulot (2011)
	Simple shear heating	Analytical solution
	Shear and adiabatic heating	Gerya (2010)
Energy + momentum	Mantle convection	Blankenbach et al. (1989), Davies et al. (2007), Gerya (2010), and Leng and Zhong (2011)
	Viscoplastic mantle convection	Tosi et al. (2015)
	Thin layer entrainment	Van Keken et al. (1997) and Thieulot (2014)
Phase changes and hydration	Hydrated sinking cylinder	Quinquis and Buiter (2014)
Melting	Experimental melting curves	Katz et al. (2003)

Note. Descriptions and results of all the benchmarks can be found in Regorda (2022).

$$\boldsymbol{\sigma} = -p\mathbf{1} + 2\eta\dot{\boldsymbol{\varepsilon}}(\vec{u}) \tag{4}$$

$$\dot{\boldsymbol{\varepsilon}}(\vec{u}) = \frac{1}{2}\left(\vec{\nabla}\vec{u} + \left(\vec{\nabla}\vec{u}\right)^{T}\right) \tag{5}$$

$$\rho(T) = \rho_0(1 - \alpha(T - T_0)) \tag{6}$$

where $\boldsymbol{\sigma}$ is the stress tensor, ρ is the density, $\vec{g}$ is the gravitational acceleration vector (pointing into the negative y-direction), $\vec{u}$ is the velocity, ρ_0 is the reference density, C_p is the isobaric heat capacity, T is the temperature, t is time, k is the thermal conductivity, H is the volumetric heat production, η is the (effective) viscosity, $\dot{\boldsymbol{\varepsilon}}$ is the strain rate tensor, α is the thermal expansion coefficient, and p is the pressure.

With an appropriate choice of boundary conditions and an initial temperature field these equations are well posed and can be numerically solved for pressure, velocity, and temperature by means of the Finite Element Method (FEM).

FALCON is a FEM code which solves Equations 1–3 in a 2D Cartesian domain. It relies on quadrilateral bilinear velocity-constant pressure elements, also coined $Q_1 \times P_0$ elements (this notation is explained for instance in Thieulot and Bangerth (2022)). $Q_1 \times P_0$ elements do not satisfy the Ladyzhenskaya, Babuska and Brezzi (LBB) stability condition (Donea & Huerta, 2003) and they are prone to element-wise checkerboard pressure pattern (van Zelst et al., 2022). Therefore, the elemental pressure is smoothed by interpolating it onto nodes and then

back onto elements centroids and markers. The code implements a so-called penalty formulation for which the flow is not truly incompressible but very weakly compressible so that Equation 2 is replaced by the following equation:

$$\vec{\nabla} \cdot \vec{u} = -\frac{p}{\lambda} \tag{7}$$

where λ is the penalty coefficient with the same units as viscosity. This then allows us to eliminate the pressure from the momentum Equation 1 resulting in the following equation:

$$\lambda \vec{\nabla}\left(\vec{\nabla} \cdot \vec{u}\right) + \vec{\nabla} \cdot \eta\left(\vec{\nabla}\vec{u} + \left(\vec{\nabla}\vec{u}\right)^T\right) + \rho\vec{g} = \vec{0} \tag{8}$$

This equation is solved for the velocity field, while the pressure can be recovered using Equation 7 as a post-processing step.

One strong requirement is that the penalty coefficient λ must be many orders of magnitude larger than the dynamic viscosity η (typically between 5 and 8 orders of magnitude). In case of large viscosity variations it has been proved beneficial to relate the penalty factor to the element's viscosity to improve the condition number of the global matrix (Dabrowski et al., 2008). A dimensionless coefficient λ^* is then used so that the penalty factor is calculated for each element as $\lambda(e) = \lambda^* \eta(e)$. Here, λ^* has been fixed to 10^6. The unfortunate consequence of the penalty method coupled to the $Q_1 \times P_0$ element is that the resulting finite element matrix is poorly conditioned and the linear system can only be solved by means of direct solvers. Therefore, FALCON relies on the parallel version of the direct MUMPS solver (Amestoy et al., 2001, 2006).

Finite element pair $Q_1 \times P_0$ has been implemented in many code used in hundreds of geodynamical publications during the last 30 years, such as ConMan (King et al., 1990), SOPALE (Fullsack, 1995), DOUAR (Braun et al., 2008), SLIM3D (Popov & Sobolev, 2008), CitcomCU (Moresi & Gurnis, 1996), CitcomS (Zhong et al., 2000), Ellipsis (O'Neill et al., 2006), Underworld (Moresi et al., 2003), FANTOM (Thieulot, 2011), and SULEC (Buiter & Ellis, 2012).

The time step is given by the Courant-Friedrichs-Lewy (CFL) condition (J. Anderson, 1995):

$$\delta t = C \min\left(\frac{h_m}{u_M}, \frac{h_m^2}{\kappa}\right) \tag{9}$$

where C is the dimensionless Courant number between 0 and 1, $h_m = \min_\Omega(h)$ is the diameter of the smallest element in the mesh, $u_M = \max_\Omega|\vec{u}|$ is the maximum velocity in the domain, and κ is the heat diffusion (typically around 1×10^{-6} m^2 s^{-1} in lithospheric-scale models).

The discretization of the equations above is standard and is available for instance in Donea and Huerta (2003), Elman et al. (2014), and in Appendix A of Thieulot (2011). At each time step δt the (nonlinear) mass and momentum conservation equations are solved, followed by the energy equation. The streamline-upwind Petrov-Galerkin (SUPG) method is implemented in the energy equation to stabilize advection (Hughes & Brooks, 1982; Thieulot, 2011). Materials are subsequently advected and topography updated.

2.1.1. Lagrangian Markers and Topography

Materials are tracked by means of the Particle-in-Cell method. A regularly distributed swarm of Lagrangian markers covers the entire domain and their advection is performed by means of a second-order Runge-Kutta scheme in space. The interpolated velocity is then corrected by means of the Conservative Velocity Interpolation (CVI), which introduces a corrective term to reduce dispersion and clustering of particles (H. Wang et al., 2015). Each particle tracks a given material type. The number of markers contained in each element is maintained between a minimum ($n_{\min}$) and a maximum ($n_{\max}$) value. When there are less markers in an element than $n_{\min}$ the code adds random markers to reach the $n_{\min}$, while if the number is higher than $n_{\max}$ some of them are randomly deleted. When new markers are added, they assume the properties of the nearest marker. In this way, elements are never empty and maintain a number of markers inside a fixed range. Elemental properties, except for the viscosity, are calculated as the arithmetic average on all the markers inside each element.

FALCON implements the Arbitrary Lagrangian Eulerian (ALE; Donea et al., 2004) formulation to accommodate topography by means of free surface deformation: the sides and bottom boundaries remain straight and the length

of the domain in the x-direction does not change (kinematic boundary conditions on these boundaries thereby imply a flux of material through the boundary). However, the top boundary deforms using the velocity field as it is resampled at equidistant abscissae with vertical adjustment of grid nodes in each column at equidistant ordinates and topography is thus created (Thieulot, 2011). To avoid the drunken-sailor instability, the free surface stabilization algorithm of Kaus et al. (2010) is implemented.

2.1.2. Rheology

The viscosities for different creep mechanisms, which are dislocation (*ds*) and diffusion (*df*) creep, are given by the following equations:

$$\eta_{ds} = A_{ds}^{-1/n_{ds}} \dot{\varepsilon}_e^{-1+1/n_{ds}} \exp\left(\frac{Q_{ds} + pV_{ds}}{n_{ds} RT}\right) \tag{10}$$

$$\eta_{df} = d^m A_{df}^{-1} \exp\left(\frac{Q_{df} + pV_{df}}{RT}\right) \tag{11}$$

(e.g., Arredondo & Billen, 2016; Billen & Hirth, 2007; Gerya et al., 2002), where A, n, Q, V are material dependent parameters. A is the preexponential factor, n is the stress exponent, Q is the activation energy, V is the activation volume, R is the gas constant, d is the grain size, m is the grain size exponent, and $\dot{\varepsilon}_e = \sqrt{I_2(\dot{\boldsymbol{\varepsilon}})}$ is the effective strain rate, given as the square root of the second invariant of the strain rate tensor. Since effects of variations of the grain size are taken into account with strain softening and healing (see below), the grain size here is constant. Note that diffusion creep is considered in the sublithospheric mantle only and in this case the stress exponent is $n = 1$, so that the corresponding viscosity does not depend on strain rate. Since both types of viscous creep act simultaneously under the same deviatoric stress (Glerum et al., 2018; Karato, 2008), the composite viscous creep η_{cp} is then calculated as the harmonic average between η_{df} and η_{ds} (e.g., Arredondo & Billen, 2016; Duretz et al., 2011; Glerum et al., 2018):

$$\eta_{cp} = \left(\frac{1}{\eta_{df}} + \frac{1}{\eta_{ds}}\right)^{-1} \tag{12}$$

To approximate brittle behavior in our models, a Drucker-Prager plasticity criterion is used (e.g., Alejano & Bobet, 2012; Glerum et al., 2018; Le Pourhiet et al., 2017; Quinquis & Buiter, 2014) and the "plastic viscosity" is then given by the following equation:

$$\eta_p = \frac{p \sin\phi + c \cos\phi}{2\dot{\varepsilon}_e} \tag{13}$$

where c is the cohesion and ϕ the angle of friction. The effective viscosity value entering the finite element matrix is then computed assuming that creep mechanisms and plasticity are independent processes (e.g., Andrews & Billen, 2009; Glerum et al., 2018; Karato, 2008), that is,

$$\eta_{\text{eff}} = \min(\eta_{cp}, \eta_p) \tag{14}$$

In order to keep this viscosity within meaningful bounds it is limited to remain in the range $[\eta_{\min}, \eta_{\max}]$, with typically $\eta_{\min} = 1 \times 10^{19}$ Pa s and $\eta_{\max} = 1 \times 10^{25}$ Pa s unless specified otherwise. The effective viscosity η_{eff} is calculated interpolating effective strain rates, pressures, and temperatures of the nodes onto the markers. Elemental viscosities are then calculated as the geometric average of η_{eff} of the markers inside each element.

Since viscosity is a function of pressure, velocity (via the strain rate), and temperature, Equation 8 is nonlinear and, although the Newton method converges faster in most cases (Fraters et al., 2019; Spiegelman et al., 2016), we resort here to the simpler so-called Picard iterations. Velocity, pressure, strain rates, and viscosities are updated at each nonlinear iteration, which are performed until either the maximum number of nonlinear iterations is reached or the normalized nonlinear residual, the velocity residual, and the pressure residual converge under a defined tolerance (Glerum et al., 2018). Here, the maximum number of iterations and the tolerance have been fixed to 100 and 10^{-3}, respectively.

Strain softening is taken into account for both plasticity and viscous creep (Babeyko & Sobolev, 2005; Huismans & Beaumont, 2003; Huismans et al., 2005; Sobolev & Babeyko, 2005; Warren et al., 2008a) by means of

the accumulated strain ε_p and ε_v, respectively, memorized by each marker. Plastic weakening approximates deformation-induced softening of faults and brittle shear zones, while viscous weakening can be interpreted as strain-induced grain size reduction and effects of synkinematic metamorphic reactions (Warren et al., 2008a). In particular, weakening due to grain size reduction has been proven important to sustain lithospheric strain localization and the development of a low-viscosity layer at the base of the lithosphere, with a consequent influence on plate tectonic evolution (Bercovici & Ricard, 2012, 2013; Dannberg et al., 2017). When the plastic strain ε_p reaches a critical value ε_1, the cohesion and angle of friction values decrease linearly with strain up until ε_p reaches another critical value ε_2 for which the cohesion and the angle of friction are now c^{sw} and ϕ^{sw}, respectively (plastic weakening). For $\varepsilon_p > \varepsilon_2$ c and ϕ remain at their strain-weakened values. In addition to the plastic weakening, all of our models include viscous weakening, which linearly reduces the viscosity by a factor f_{vw} up to 10 when the viscous strain ε_v is between ε_1 and ε_2 (Huismans & Beaumont, 2003; Warren et al., 2008a). This value of f_{vw} is in agreement with suggestion from laboratory experiments on monomineralic systems and field studies of polymineralic systems (Warren et al., 2008a).

At each time step δt the accumulated strain ε_t, both plastic and viscous, is calculated as follows:

$$\varepsilon_t = \varepsilon_{t-1} + (\dot{\varepsilon}_e - \varepsilon_{t-1} H_{\text{rate}}(T))\delta t \tag{15}$$

with the temperature-dependent healing factor $H_{\text{rate}}(T)$ defined as follows:

$$H_{\text{rate}}(T) = B\exp\left[-\frac{\mu_H}{2}\left(\frac{1}{T^* + 1} - \frac{1}{2}\right)\right] \tag{16}$$

where B is a constant describing the timescale of healing, while μ_H and $T^* = \frac{T - T_s}{T_b - T_s}$ are the nondimensional temperature activation and temperature, respectively (Fuchs & Becker, 2021), with T_b and T_s the temperatures at the bottom and at the surface of the domain.

2.1.3. Melting

Melt fraction in the mantle depends on temperature (T, in °C), total pressure (p, in GPa), and the water content in the melt (X_{H_2O}, in wt.%). The determination of the melt fraction M is implemented as explained by Katz et al. (2003), according to the successive modification by Langmuir et al. (2006) and Kelley et al. (2010), as follows:

$$M\left(p, T, X_{H_2O}\right) = -T + T_{sol} + (x_t \cdot \ln(p + y_t)) \cdot X_{H_2O} - \\ + K_m\left(\frac{X_{H_2O}^{bulk}}{D_{H_2O}\left(1 - X_{H_2O}\right) + X_{H_2O}}\right)^{\gamma} \tag{17}$$

where T_{sol} is the temperature of the dry solidus, D_{H_2O} is the partition coefficient, $x_t \cdot \ln(p + y_t)$ indicates the pressure dependence of the melting curve, and K_m and γ are parameters needed to calculate the temperature decrease in the solidus caused by a water content. Values and meanings of the parameters x_t, y_t, K_m, and γ are described in Katz et al. (2003) and Kelley et al. (2010). X_{H_2O} depends on the melt fraction as follows:

$$X_{H_2O}(M) = \frac{X_{H_2O}^{bulk}}{D_{H_2O} + M\left(1 - D_{H_2O}\right)} \tag{18}$$

and a numerical solution can be found using a root-finder method (Kelley et al., 2010; Z. Wang et al., 2016). Furthermore, the content of water in the melt is limited by the pressure-dependent saturation concentration of water in the melt, determined as follows:

$$X_{H_2O}^{sat} = \chi_1 p^{\lambda_m} + \chi_2 p \tag{19}$$

where χ_1, χ_2, and λ_m are parameters chosen according to Katz et al. (2003), Langmuir et al. (2006), and Kelley et al. (2010). In case of melting, rheological weakening of the viscous creep viscosity η_{cp} is taken into account according to Z. Wang et al. (2016), as follows:

$$\eta_{cp} = \eta_{cp} \cdot e^{(\alpha_m M)} \tag{20}$$

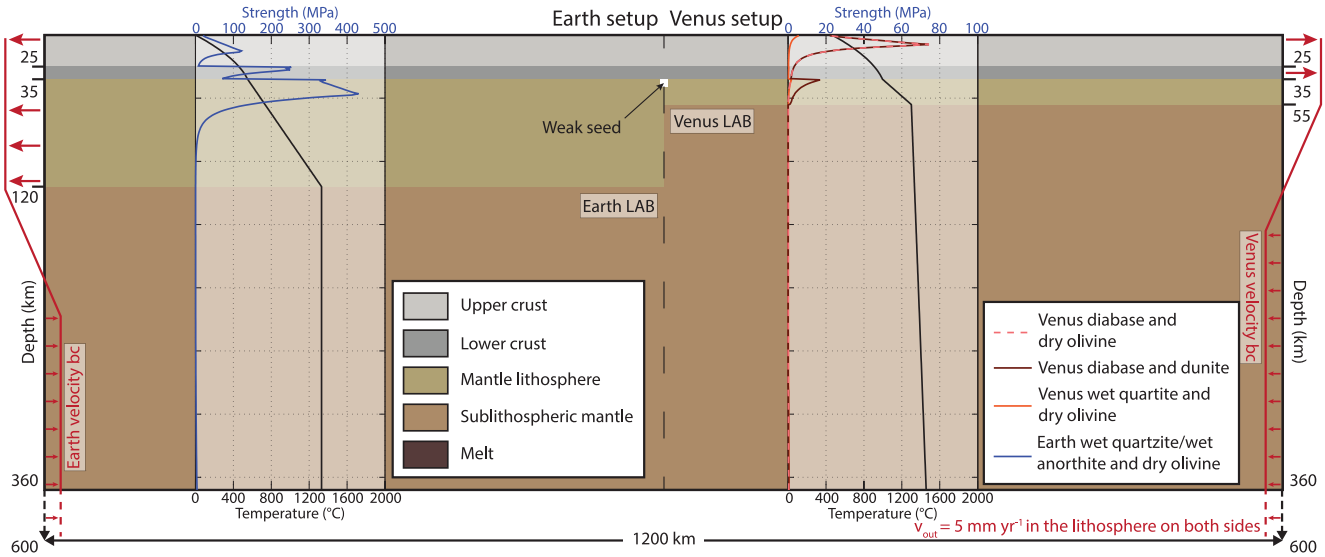

Figure 2. Model setup showing crust and mantle lithosphere layer thicknesses and the corresponding strength and temperature profiles, the weak seed to initialize localization, and the velocity boundary conditions (red) for our initial Earth model (left) and the Venus setup (right). Strength profiles are calculated far from the weak seed at the beginning of the evolution with the strain rates resulting from a divergence velocity of 1 cm (approximately 5×10^{-15} s^{-1}).

where α_m is the melt fraction factor for dislocation and diffusion creep. The effective density (ρ_{eff}) for partially molten rocks is calculated as follows:

$$\rho_{\text{eff}} = \rho_s(1 - M) + \rho_m M \tag{21}$$

where ρ_s and ρ_m are the densities of the solid and the molten rock, respectively (Gerya & Yuen, 2007; Gerya et al., 2004; Z. Wang et al., 2016).

2.2. Numerical Setup

In this study, we use two different setups for Earth and Venus (Figure 2) with an experimental domain of 1,200 × 600 km. The minimum numerical resolution is 5 × 5 km with a horizontal refinement toward the center of the model (between $x = 400$ and $x = 800$ km) and a vertical refinement toward the surface (above 120 km depth) where the maximum resolution is 1 × 1 km. The total number of elements is 163,200 and each element is initialized with 16 markers that allow for the tracking of different materials throughout the experiments. For time stepping we use the CFL condition with a Courant number of 0.05 and a maximum time step of 10 kyr. Such a low value of the Courant number has been chosen to avoid the drunken sailor effect in case of the low viscosities predicted by the models in case of the high surface temperature of Venus.

In the Earth setup, we consider a 25 km thick upper crust, a 10 km thick lower crust, and an 85 km thick layer of lithospheric mantle resulting in a 120 km thick lithosphere on top of the asthenosphere. In contrast, in the Venus setup we consider a 35 km thick crust, as for the Earth, at the top of a lithospheric mantle that is only 20 km thick, similarly to the lithospheric structure used in previous numerical models of Venus (Gerya, 2014; Gülcher et al., 2020). In case of the Venus setup, we also tested models with no lower crust (e.g., F. S. Anderson & Smrekar, 2006; Gudkova & Zharkov, 2020; Kiefer & Peterson, 2003; Sandwell et al., 1997; Simons et al., 1997; Xiao et al., 2020), resulting in a 25 km thick crust and a 20 km thick lithospheric mantle. For the sake of simplicity, we did not consider any phase transition neither in the crust nor in the mantle. Measurements of Venusian crustal rocks indicated a predominantly basaltic composition (Foster & Nimmo, 1996; Mackwell et al., 1998), similar to terrestrial oceanic rocks. Therefore, we test for the crust both a classic terrestrial rheology (wet quartzite and wet anorthite for the upper and the lower crust, respectively; e.g., Farangitakis et al., 2020; Naliboff & Buiter, 2015; Peron-Pinvidic et al., 2022) and a dry diabase flow law to represent both the upper and the lower crust of Venus (e.g., Byrne et al., 2021; Kohlstedt & Mackwell, 2009; Mackwell et al., 1998). In fact, dry diabase is characterized by a stronger rheology than wet quartzite and it is often used in numerical modeling studies of long-term tectonic processes as a rheology for the oceanic crust (e.g., Auzemery et al., 2020; Sleep & Warren, 2014; Warren

et al., 2008a). Here, we used the Maryland diabase flow law from Mackwell et al. (1998) to simulate a stronger rheology due to the absence of water hypothesized for Venus' interiors (Foster & Nimmo, 1996). Although some studies have tried to constrain mantle viscosity on Venus by means of the long-wavelength geoid (Benešová & Čížková, 2012; Pauer et al., 2006; Rolf, Steinberger, et al., 2018), some uncertainties still remain (Aitta, 2012; Armann & Tackley, 2012). Therefore, we decide to investigate the effects of two different rheologies for both the lithospheric and the asthenospheric mantle. In particular we test a dry olivine, as widely used for models of Earth (e.g., Brune et al., 2017; Gerya, 2013; Korenaga, 2013), and a stronger dry dunite, as assumed by some authors for Venus (e.g., Byrne et al., 2021; Ghail, 2015). The rheological parameters of each of these layers can be found in Table 2.

In order to localize deformation in the center of the model domain, we used and tested 3 different types of weak seeds. Type one is a 6×6 km strain-weakened domain located at the top of the lithospheric mantle. Type two is a 6×6 km strain-weakened domain located at the strong part of the upper-crust, and, since this seed is extremely shallow, we also tested a smaller 2×2 km seed to minimize its effect at surface. Type three is a random Gaussian distribution of strain assigned only to lithospheric markers, according to the following equation:

$$\varepsilon = \mathrm{rdm}(\varepsilon_1, \varepsilon_2) \exp\left(-\frac{(x-\mu)^2}{2\sigma^2}\right) \tag{22}$$

where $\mathrm{rdm}(\varepsilon_1, \varepsilon_2)$ is a random number between ε_1 and ε_2, x is the horizontal coordinate of the marker, and μ and σ are the mean and the standard deviation of the Gaussian distribution, respectively. Here, the distribution of the initial strain assigned to each marker has been centered in the middle of the domain ($\mu = 600$ km) and spread out over a range of 4σ, with $\sigma = 150$ km.

Depending on the model setup, the initial temperature-profile is either a steady-state geotherm characteristic of the continental lithosphere on Earth with a fixed surface temperature of 0°C and a basal temperature of 1330°C at 600 km depth (e.g., Erdős et al., 2019; Marotta et al., 2020; Regorda et al., 2021), or a steady-state geotherm characteristic of Venus with a fixed surface temperature of 464°C and a basal temperature of 1580°C at 600 km depth (e.g., Gudkova & Zharkov, 2020; Gülcher et al., 2020). At the start of the model, a constant outflow velocity of 0.5 cm yr^{-1} is set along both vertical boundaries from the surface down to the bottom of the lithosphere, resulting in a total extension rate of 1 cm yr^{-1}, in agreement with estimates by Ghail (2015). A constant inflow velocity along the vertical boundaries in the asthenosphere and a linear transitional zone of 100 km is set such that the net material flux along the vertical boundaries is 0. Apart from the lithospheric setup, the initial seeding and the initial temperature profile, we also vary the value of gravitational acceleration and the surface pressure to correspond to Venus surface conditions. All the simulations tested are summarized in Table 3.

3. Results

First of all, we here present the modeling results of a model with terrestrial conditions and without viscous weakening, followed by the results of a similar model but with the addition of the viscous weakening. Since the rheology of Venus is largely unconstrained, we here present the modeling results for three different proposed rheologies. For each rheology, we consider the impact of the Venusian surface pressure, gravitational acceleration, and lithospheric temperature profile. For these models, we considered a duration of the extension of 10 Myr. In addition, we present the results of the effects of different types of weak seeds and crustal thicknesses on models with Venusian conditions and for each rheology. We tested these models for a maximum duration of the extension up to 20 Myr to guarantee the potential strain accumulation and the consequent development of the rifting. First, we discuss the results of a typical terrestrial rheology with wet quartzite and wet anorthite for the upper and lower crust, respectively, and a dry olivine rheology for the mantle. Second, we consider a diabase rheology for both the upper and lower crust and dry olivine for the mantle. Last, we consider a diabase rheology for the crust and a dry dunite rheology for the mantle.

In the figures presented throughout this work, the models are identified by their unique model identifier (first column of Table 3) and by the parameters that are modified with respect to the Earth model: *P* indicates the use of the Venusian surface pressure (9.3 MPa; e.g., Gudkova & Zharkov, 2020), *g* indicates the use of the Venusian gravitational acceleration (8.87 m s^{-2}), *T* indicates the use of the Venusian temperature profile, *L* indicates a 55 km-thick Venusian lithosphere, and *C* indicates a 25 km-thick crust instead of the reference case of 35 km

Journal of Geophysical Research: Planets

10.1029/2022JE007588

Table 2
Densities and Plastic, Viscous, and Thermal Parameters of the Materials Used in the Models

Parameter	Symbol	Units	Upper crust		Lower crust		Lithospheric mantle		Sublithospheric mantle	
Thickness	–	km	25		0–10		20–85		480–545	
Density[a,b]	ρ	kg m^{-3}	2,800	2,900	2,950	2,900	3,300 (2,900)	3,300 (2,900)	3,300 (2,900)	3,300 (2,900)
Friction angle	ϕ	°	25–5	25–5	25–5	25–5	25–5	25–5	25–5	25–5
Cohesion[c]	c	MPa	20–4	20–4	20–4	20–4	20–4	20–4	20–4	20–4
Viscous weakening factor[d]	f_{vw}	–	10	10	10	10	10	10	10	10
Strain weakening range[e]	$\varepsilon_1 - \varepsilon_2$	–	0–1	0–1	0–1	0–1	0–1	0–1	0–1	0–1
Flow law			Wet quartzite[a,f]	Dry Maryland diabase[b,g]	Wet anorthite[a,h]	Dry Maryland diabase[b,g]	Dry olivine[a,i]	Dry dunite[j,k]	Dry olivine[a,i]	Dry dunite[j,k]
Dislocation creep										
Preexponential factor	A_{ds}	(Pa s^{-1})	8.57×10^{-28}	5.05×10^{-28}	7.13×10^{-18}	5.05×10^{-28}	6.52×10^{-16}	1.13×10^{-21}	6.52×10^{-16}	1.13×10^{-21}
Stress exponent	n_{ds}	–	4	4.7	3	4.7	3.5	3.6	3.5	3.6
Activation energy	Q_{ds}	(kJ mol^{-1})	223	485	345	485	530	535	530	535
Activation volume	V_{ds}	(m^3 mol^{-1})	0	0	0	0	1.8×10^{-5}	1.8×10^{-5}	1.8×10^{-5}	1.8×10^{-5}
Diffusion creep										
Preexponential factor	A_{df}	(Pa s^{-1})	–	–	–	–	–	–	2.37×10^{-15}	1.5×10^{-15}
Activation energy	Q_{df}	(kJ mol^{-1})	–	–	–	–	–	–	375	375
Activation volume	V_{df}	(m^3 mol^{-1})	–	–	–	–	–	–	1×10^{-5}	1×10^{-5}
Grain size	d	(mm)	–	–	–	–	–	–	5	5
Grain size exponent	m	–	–	–	–	–	–	–	3	3
Thermal parameters										
Heat capacity[b,l]	C_p	(m^2 K s^{-2})	800		800		1,250		1,250	
Conductivity[a,b]	k	(W m^{-1} K^{-1})	2.5		2.5		2.25		2.25	
Thermal expansion[b,m]	α	(K^{-1})	3×10^{-5}		3×10^{-5}		3×10^{-5}		3×10^{-5}	
Heat production[b]	H	(μW m^{-2})	1.3		1.3		0		0	

Note. For each material, the left column contains the reference rheology representative of a normal continental lithosphere on Earth, while the right column contains the alternative rheologies assumed for the lithosphere of Venus. Mantle densities in brackets refer to the melt densities.

[a]Naliboff and Buiter (2015). [b]Warren et al. (2008b). [c]Erdős et al. (2014). [d]Huismans and Beaumont. [e]Naliboff et al. (2017). [f]Rutter and Brodie (2004). [g]Mackwell et al. (1998). [h]Rybacki et al. (2006). [i]Hirth and Kohlstedt (2003). [j]Chopra and Paterson (1981). [k]Burov (2011). [l]Tetreault and Buiter (2018). [m]Rolf, Capitanio, and Tackley (2018).

Table 3
Simulations

Model	UC rheology	LC rheology	Mantle rheology	Viscous weakening	Surface pressure (MPa)	Gravity (m s^{-2})	Lithospheric temperature (°C)	Lithospheric thickness (km)	Crustal thickness (km)	Weak seed	Model time (Myr)	Figures
R1	Quartzite	Anorthite	Olivine	1	0	9.81	0–1330	120	35	Mantle	10	Figure 3
Q1	Quartzite	Anorthite	Olivine	10	0	9.81	0–1330	120	35	Mantle	10	Figure 4
Q2	Quartzite	Anorthite	Olivine	10	9.3	9.81	0–1330	120	35	Mantle	10	Figure 5
Q3	Quartzite	Anorthite	Olivine	10	0	8.87	0–1330	120	35	Mantle	10	Figure 5
Q4	Quartzite	Anorthite	Olivine	10	9.3	8.87	0–1330	120	35	Mantle	10	Figure 5
Q5	Quartzite	Anorthite	Olivine	10	0	9.81	464–1300	55	35	Mantle	10	Figure 5
Q6	Quartzite	Anorthite	Olivine	10	9.3	9.81	464–1300	55	35	Mantle	10	–
Q7	Quartzite	Anorthite	Olivine	10	0	8.87	464–1300	55	35	Mantle	10	–
Q8	Quartzite	Anorthite	Olivine	10	0	9.81	464–1300	120	35	Mantle	10	Figure 5
Q9	Quartzite	Anorthite	Olivine	10	9.3	8.87	464–1794	120	35	Mantle	–	–
Q10	Quartzite	Anorthite	Olivine	10	9.3	8.87	464–1300	55	35	Mantle	20	–
Q11	Quartzite	Anorthite	Olivine	10	9.3	8.87	464–1300	55	35	Crust (2 × 2)	20	–
Q12	Quartzite	Anorthite	Olivine	10	9.3	8.87	464–1300	55	35	Crust (6 × 6)	20	Figure 6
Q13	Quartzite	Anorthite	Olivine	10	9.3	8.87	464–1300	55	35	Random	20	Figure 6
Q14	Quartzite	–	Olivine	10	9.3	8.87	464–1300	55	25	Mantle	20	Figure 6
Q15	Quartzite	–	Olivine	10	9.3	8.87	464–1300	55	25	Crust (2 × 2)	20	–
Q16	Quartzite	–	Olivine	10	9.3	8.87	464–1300	55	25	Crust (6 × 6)	20	–
Q17	Quartzite	–	Olivine	10	9.3	8.87	464–1300	55	25	Random	20	–
D1	Diabase	Diabase	Olivine	10	0	9.81	0–1330	120	35	Mantle	10	Figure 7
D2	Diabase	Diabase	Olivine	10	9.3	9.81	0–1330	120	35	Mantle	10	–
D3	Diabase	Diabase	Olivine	10	0	8.87	0–1330	120	35	Mantle	10	–
D4	Diabase	Diabase	Olivine	10	0	9.81	464–1300	55	35	Mantle	10	–
D5	Diabase	Diabase	Olivine	10	9.3	8.87	464–1300	55	55	Mantle	20	Figure 8
D6	Diabase	Diabase	Olivine	10	9.3	8.87	464–1300	55	35	Crust (2 × 2)	20	–
D7	Diabase	Diabase	Olivine	10	9.3	8.87	464–1300	55	35	Crust (6 × 6)	20	Figure 8
D8	Diabase	Diabase	Olivine	10	9.3	8.87	464–1300	55	35	Random	20	Figure 8
D9	Diabase	–	Olivine	10	9.3	8.87	464–1300	55	25	Mantle	20	Figure 9
D10	Diabase	–	Olivine	10	9.3	8.87	464–1300	55	25	Crust (2 × 2)	20	–
D11	Diabase	–	Olivine	10	9.3	8.87	464–1300	55	25	Crust (6 × 6)	8	Figure 9
D12	Diabase	–	Olivine	10	9.3	8.87	464–1300	55	25	Random	10	Figure 9
DD1	Diabase	Diabase	Dunite	10	0	9.81	0–1330	120	35	Mantle	10	Figure 10
DD2	Diabase	Diabase	Dunite	10	9.3	9.81	0–1330	120	35	Mantle	10	–
DD3	Diabase	Diabase	Dunite	10	0	8.87	0–1330	120	35	Mantle	10	–
DD4	Diabase	Diabase	Dunite	10	0	9.81	464–1300	55	35	Mantle	10	–
DD5	Diabase	Diabase	Dunite	10	9.3	8.87	464–1300	55	35	Mantle	20	Figure 11
DD6	Diabase	Diabase	Dunite	10	9.3	8.87	464–1300	55	35	Crust (2 × 2)	20	–
DD7	Diabase	Diabase	Dunite	10	9.3	8.87	464–1300	55	35	Crust (6 × 6)	20	Figure 11
DD8	Diabase	Diabase	Dunite	10	9.3	8.87	464–1300	55	35	Random	20	Figure 11
DD9	Diabase	–	Dunite	10	9.3	8.87	464–1300	55	25	Mantle	10	Figure 12
DD10	Diabase	–	Dunite	10	9.3	8.87	464–1300	55	25	Crust (2 × 2)	20	–

Table 3
Continued

Model	UC rheology	LC rheology	Mantle rheology	Viscous weakening	Surface pressure (MPa)	Gravity (m s^{-2})	Lithospheric temperature (°C)	Lithospheric thickness (km)	Crustal thickness (km)	Weak seed	Model time (Myr)	Figures
DD11	Diabase	–	Dunite	10	9.3	8.87	464–1300	55	25	Crust (6 × 6)	20	Figure 12
DD12	Diabase	–	Dunite	10	9.3	8.87	464–1300	55	25	Random	20	Figure 12

Note. The following parameters have been varied: upper crust (UC), lower crust (LC), mantle rheology, surface pressure, gravitational acceleration, lithospheric temperature and thickness, crustal thickness, type of weak seed, and the duration of the evolution. The models are shown in the figures listed in the last column.

(e.g., the identifier *Pg* will be used in case of a model with only pressure and gravity of Venus). When we use all assumed Venusian conditions, that is its surface pressure, gravitational acceleration, temperature profile, and lithosphere thickness, the identifier *V* is used instead to indicate a full Venusian model. In addition, in case of Venus conditions, *.m*, *.c*, and *.r* are used to identify mantle, crustal, and random weak seeds, respectively (e.g., the identifier *VC.r* will be used in case of a model with pressure, gravity, and temperature conditions of Venus and with both a 25 km-thick crust and a random seed).

3.1. Models With a Wet Quartzite/Wet Anorthite Rheology in the Crust and Dry Olivine in the Mantle

3.1.1. Earth Model Without Viscous Weakening—Model R1

Our model with typical pressure and temperature conditions of the Earth and without viscous weakening (model R1) shows the classical formation of symmetric shear bands with high strain rates in correspondence of the imposed weak seed (Figure 3a). Localization of high strain rates produces low viscosities inside the symmetric shear bands (Figures 3d–3f) and a continuous accumulation of plastic strain that allows the development of symmetric conjugate normal faults along which the extension is accommodated (Figures 3h and 3i). The symmetric evolution is observed during the whole numerical experiment and is characterized by a continuous upwelling of the mantle associated with a slight crustal thinning during the first 10 Myr of evolution (Figure 3h) and a

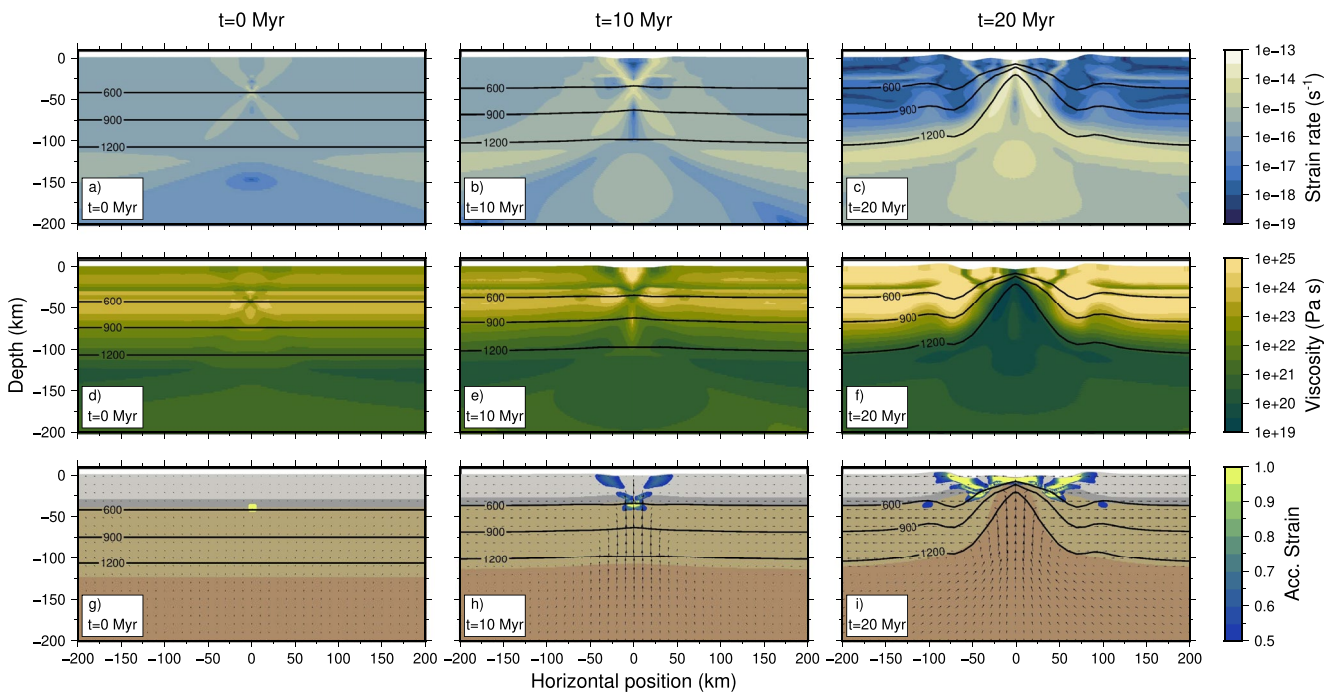

Figure 3. Evolution of strain rates (first row), viscosities (second row), and composition (third row) with accumulated strain of model R1 without viscous weakening at 0 Myr (left column), 10 Myr (middle column) and 20 Myr (right column). Note that the accumulated strain is shown only if $\varepsilon_t > 0.5$. Black lines represent 600, 900, and 1200°C isotherms. Background colors are defined by the composition in panels (g–i) as in Figure 2.

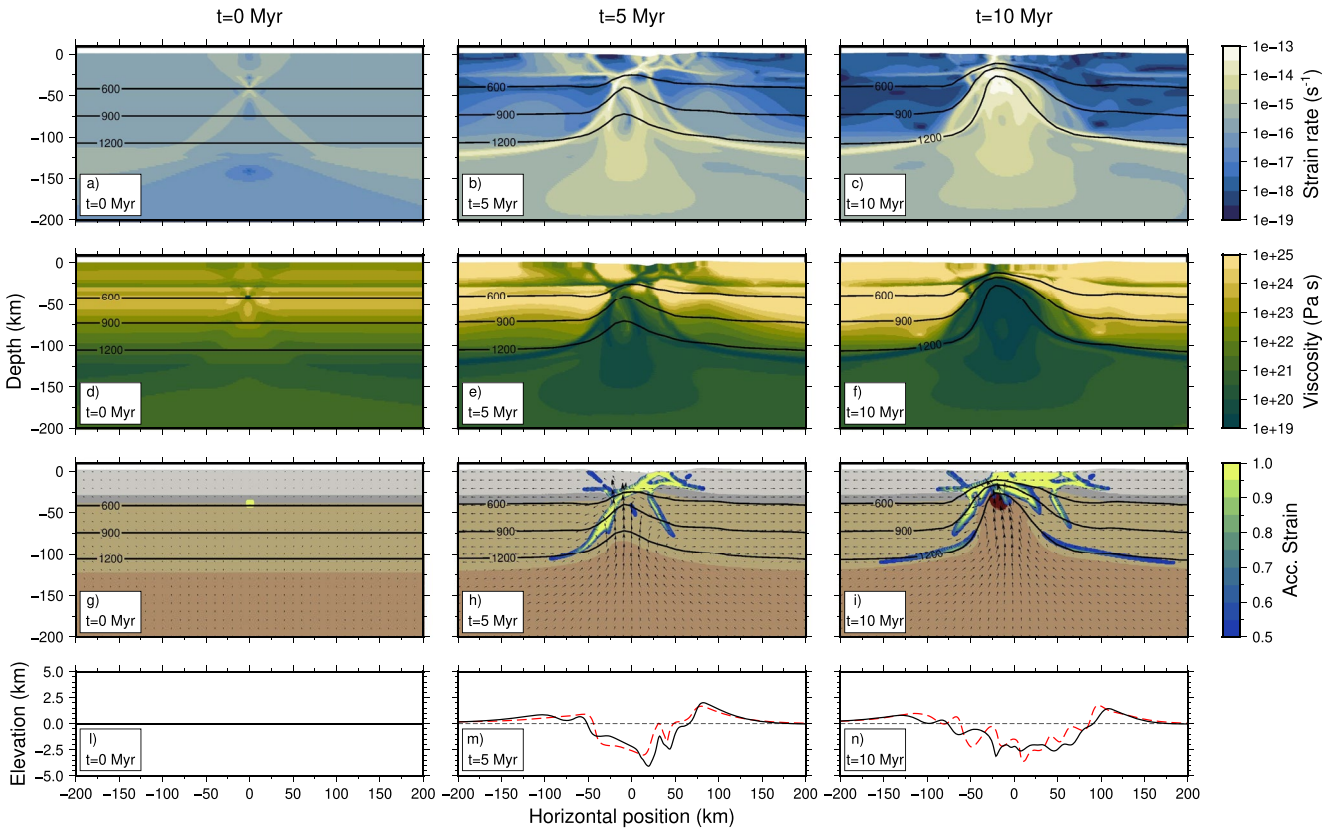

Figure 4. Evolution of strain rates (first row), viscosities (second row), and composition (third row) with accumulated strain of model Q1 with conditions of the Earth and wet quartzite/wet anorthite rheologies for the upper/lower crust and dry olivine in the mantle at 0 Myr (left column), 5 Myr (middle column), and 10 Myr (right column). Note that the accumulated strain is shown only if $\varepsilon_t > 0.5$. Black lines in panels (a–i) represent 600, 900, and 1200°C isotherms. Background colors are defined by the composition in panels (g–i) as in Figure 2; dark brown indicates melt. Continuous and dashed black lines in panels (l–n) represent the topography and the initial topography, respectively; dashed red lines in panels (l–n) represent topography of model R2 with modified plastic and weakening parameters.

successive crustal break up at 19–20 Myr (Figure 3i and Movies S3 and S4 in Supporting Information S1) when the lithospheric mantle is exposed. In this model, we do not account for melting to recreate at best the conditions of previous numerical models (e.g., Beucher & Huismans, 2020; Naliboff & Buiter, 2015).

3.1.2. Earth Model—Model Q1

Our reference model with the surface pressure, gravitational acceleration, and temperature profile of the Earth and the introduction of the viscous weakening (model Q1) initially shows the formation of symmetric shear bands with high strain rates (Figure 4a), as observed in the model R1. However, it soon evolves into an asymmetric rift (Figures 4h and 4i and Movies S1 and S2 in Supporting Information S1). The effects of the viscous weakening are clear in the lithospheric mantle, resulting in very high strain rates and lower viscosities than model R1 (Figures 4c and 4f, respectively) where the strain accumulates (Figure 4i), even if the temperature-dependent viscous healing allows the strain to accumulate only along narrow areas characterized by very high strain rates.

Apart from the general asymmetric evolution, model Q1 shows a continuous upwelling of the mantle associated with crustal thinning but no crustal break up is observed at the end of the evolution after 10 Myr (Figure 4i). However, the abundant mantle upwelling results in partial melting of approximately 7% in the shallow portion of the asthenosphere after 9–10 Myr of evolution (dark brown in Figure 4i).

The evolution of model Q1 results in an asymmetric topography characterized by different heights on the opposite sides of the rifting. In particular, heights on the left side of model do not change during the evolution with a maximum value of 800 m (Figures 4m and 4n), while on the right side the maximum height is approximately 1,500 m with a slight decrease in time (Figures 4m and 4n). Similarly, the continental basin is characterized by an asymmetric topography with a decrease of the maximum depth throughout the evolution and a maximum depth of approximately 2,500 m at the end of the numerical experiment. We performed a model to test the effects

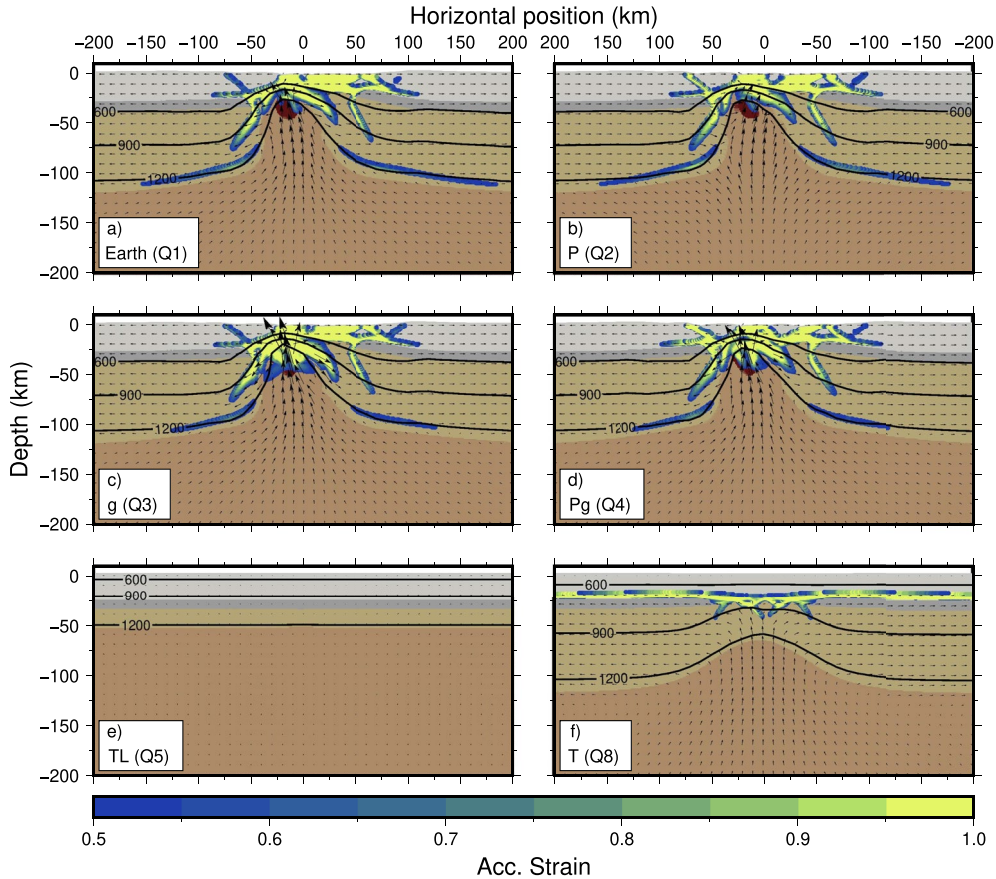

Figure 5. Final distribution of composition and accumulated strain of models with wet quartzite and wet anorthite rheologies for the upper and lower crust and a dry olivine rheology for the mantle at 10 Myr. (a) Model of the Earth (model Q1); (b) model with surface pressure of Venus (P, model Q2); (c) model with gravitational acceleration of Venus (g, model Q3); (d) model with surface pressure and gravitational acceleration of Venus (Pg, model Q4); (e) model with temperature profile and lithospheric thickness of Venus (TL, model Q5); and (f) model with temperature profile of Venus but lithospheric thickness of Earth (T, model Q8). Note that the accumulated strain is shown only if $\varepsilon_t > 0.5$. Black lines represent 600, 900, and 1200°C isotherms. Background colors are defined by the composition as in Figure 2; dark brown indicates melt.

of different plastic and weakening parameters on the overall evolution (model R2). We observe that different initial/final cohesion and friction angle (20/4 MPa and 15°/2°, respectively) and different weakening parameters ($\varepsilon_1 = 0.1$ and $\varepsilon_2 = 0.6$) produce a very similar large-scale final geometry (Movies S3bis and S4bis in Supporting Information S1) and the same final topography (dashed red lines in Figures 4l–4n), even if with a slight slower evolution. In fact, the final setting at 10 Myr of model R2 is equivalent to the setting at 7 Myr of model Q1.

3.1.3. Effects of Venusian Surface Conditions: Pressure, Gravitational Acceleration, and Temperature—Models Q2–Q9

The effects of separately including the surface pressure and gravitational acceleration of Venus into the Earth model on the evolution of a continental rift have been tested systematically in models Q2 and Q3 and have then been combined in model Q4.

We observe that neither the increased surface pressure nor the lowered gravitational acceleration play an essential role on the evolution, showing almost identical areas of accumulated strain and very similar amounts of mantle upwelling and crustal thinning (Figures 5b–5d). However, some differences can be observed in the extent of the melting area. In particular, the higher Venusian surface pressure combined with the gravitational acceleration of the Earth (model Q2) results in higher pressures in the Venus interior, with less mantle melting as a consequence (dark brown in Figure 5b). Specifically, conditions of pressure and temperature compatible with mantle melting occur in 286 elements and a maximum melt fraction of 6% for model Q2 with respect to 346 elements and a maximum melt fraction of 7% for model Q1. On the contrary, models with the lower gravitational acceleration

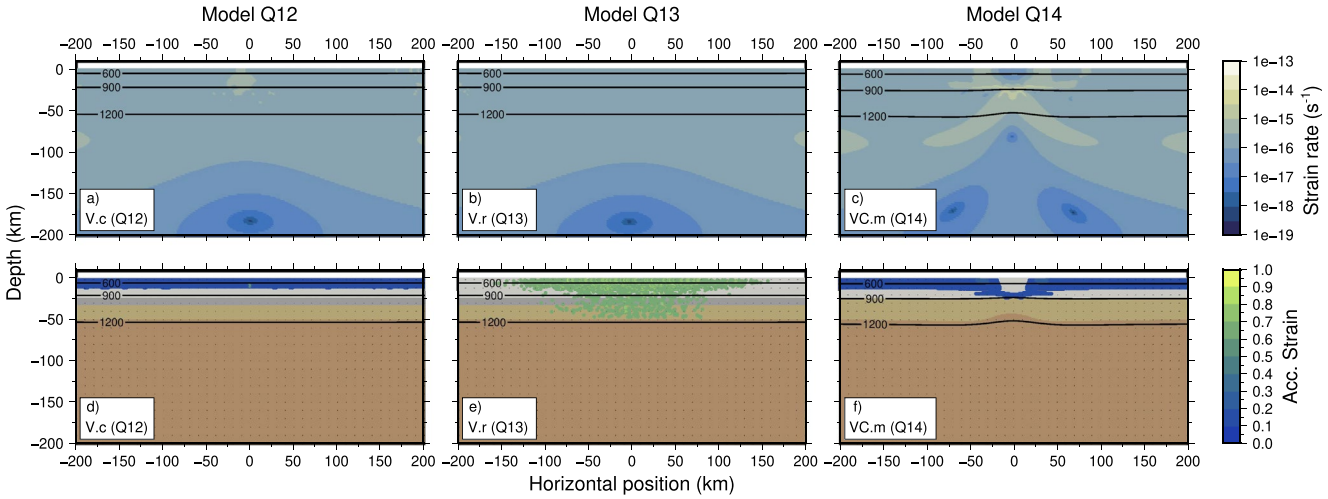

Figure 6. Final distribution of strain rates (first row) and composition with accumulated strain (second row) of models with Venus conditions and wet quartzite and wet anorthite rheologies for the upper and lower crust and a dry olivine rheology for the mantle after 20 Myr. 6 × 6 km crustal seed and 35 km-thick crust model (V.c in the left column; model Q12); random seed and 35 km-thick crust model (V.r in the middle column; model Q13); mantle seed with 25 km-thick crust model (VC.m in the right column; model Q14). Black lines represent 600, 900, and 1200°C isotherms. Background colors are defined by the composition in panels (d–f) as in Figure 2.

of Venus (models Q3 and Q4) show larger areas of melting with 661 and 511 elements, respectively, and a maximum melt fraction of 11% (dark brown in Figures 5c and 5d), as a response to the reduced pressure conditions compared to the reference model (model Q1). In particular, the gravitational acceleration of Venus results in reduced pressure below 3.5 km even when combined with the higher surface pressure.

In contrast to the minimal effects of varying the pressure and gravitational acceleration of Venus, changing the temperature profile of the lithosphere (models Q5 to Q9) has a big impact on the general rift evolution. In fact, the high surface temperature of Venus determines a clear different strength profile in the crust, with the disappearance of the brittle layer (continuous red line in the strength profile of Venus in Figure 2). Therefore, these high temperatures in combination with a 55 km-thick lithosphere do not allow for the development of shear bands at the beginning of the evolution, preventing strain localization and the development of a continental rift (Figure 5e). The same behavior is also observed when the temperature profile of Venus is combined with the surface pressure (model Q6) and gravitational acceleration (model Q7) of Venus. Surface temperature of Venus combined with a 120 km-thick lithosphere (model Q8) results in a lower thermal gradient (see isotherms in Figure 5), with consequent lower temperatures with respect to models with a thinner lithosphere (models Q5–Q7). This thermal profile allows for the development of shear bands at the interface between the upper and lower crust and deeper in the lithospheric mantle, with the consequent localization and accumulation of strain (Figure 5f). This behavior results in mantle deformation and upwelling, even if less pronounced than in models Q1–Q4, but no melting (Figure 5f). However, there are no traces of shear bands and accumulated strain in the shallower portion of the upper crust and no crustal thinning is observed (Figure 5f).

One last test has been conducted using the surface temperature of Venus in combination with a thermal gradient of the Earth in a 120 km-thick lithosphere (model Q9). In this case, however, the temperatures at the bottom of the lithosphere are so high that the entire sublithospheric mantle is under melting conditions. Therefore, the model could not be run beyond a few hundreds of years since the low viscosity of the melt in such a large area results in very high velocities and therefore small time steps on the order of a few years.

3.1.4. Venus Models—Models Q10–Q17

In our Venus models, we test crustal thicknesses of 35 (models Q10–Q13) and 25 km (models Q14–Q17) and additional kinds of weak seeds to see how strain can localize under Venusian conditions. In particular, we test two different weak seeds in the upper crust, one with dimensions 2 × 2 km (models Q11 and Q15) and one with dimensions 6 × 6 km (models Q12 and Q16), in addition to a model with diffuse random seeding (models Q13 and Q17).

In case of a 35 km-thick crust, we observe that when the temperature profile of Venus is combined with the Venusian surface pressure and gravitational acceleration, there is no strain localization with any kind of weak seed (models Q10–Q13), even after 20 Myr of evolution. In all these models the high temperatures prevent the

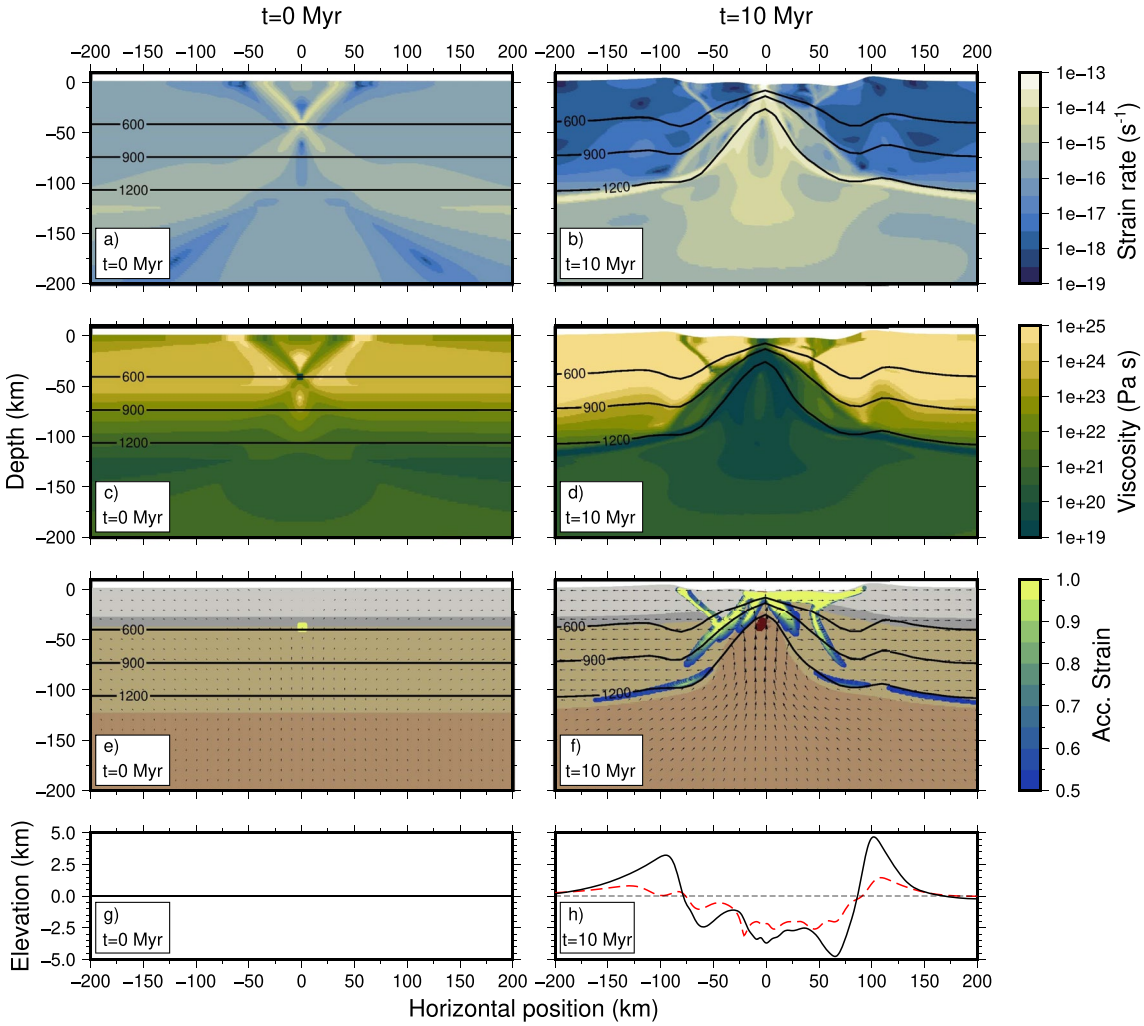

Figure 7. Evolution of strain rates (first), viscosities (second row), and composition with accumulated strain (third row) of model D1 with Earth conditions and a diabase rheology for the crust and a dry olivine rheology for the mantle at 0 Myr (left column) and 10 Myr (right column). Note that the accumulated strain is shown only if $\varepsilon_{ii} > 0.5$. Black lines in panels a–f represent 600, 900, and 1200°C isotherms. Background colors are defined by the composition in panels (e and f) as in Figure 2; dark brown indicates melt. Continuous and dashed black lines in panels (g and h) represent the topography and the initial topography, respectively; dashed red line in panels (g and h) represent topography of model Q1.

development of shear bands (model Q12 in Figure 6a and model Q13 in Figure 6b), and the development of a rift is impeded by the lack of strain localization (model Q12 in Figure 6d and model Q13 in Figure 6e).

In the case of a crustal thickness of 25 km in combination with Venus conditions (models Q14–Q17), models show higher strain rates (model Q14 in Figures 6c and 6f) than in models with a thicker crust. As a consequence, some strain localization is observed in the crust, as well as the beginning of a mantle upwelling in the model with a mantle weak seed after 20 Myr of evolution (model Q14 in Figure 6f). The models with different seeds (models Q15-Q17) do not show any deformation, similar to the models with 35 km-thick crust.

3.2. Models With a Diabase Rheology in the Crust and Dry Olivine in the Mantle

In the following models, we choose a diabase flow law to represent both the upper and the lower crust of Venus (e.g., Byrne et al., 2021; Kohlstedt & Mackwell, 2009; Mackwell et al., 1998).

3.2.1. Earth Model and Effects of Venusian Surface Conditions: Pressure, Gravitational Acceleration, and Temperature—Models D1–D4

The use of a diabase flow law (model D1) for the crust results in higher viscosities throughout the entire evolution of the model, in particular in the lower crust, compared to our other models of Earth (compare Figures 7c and 7d

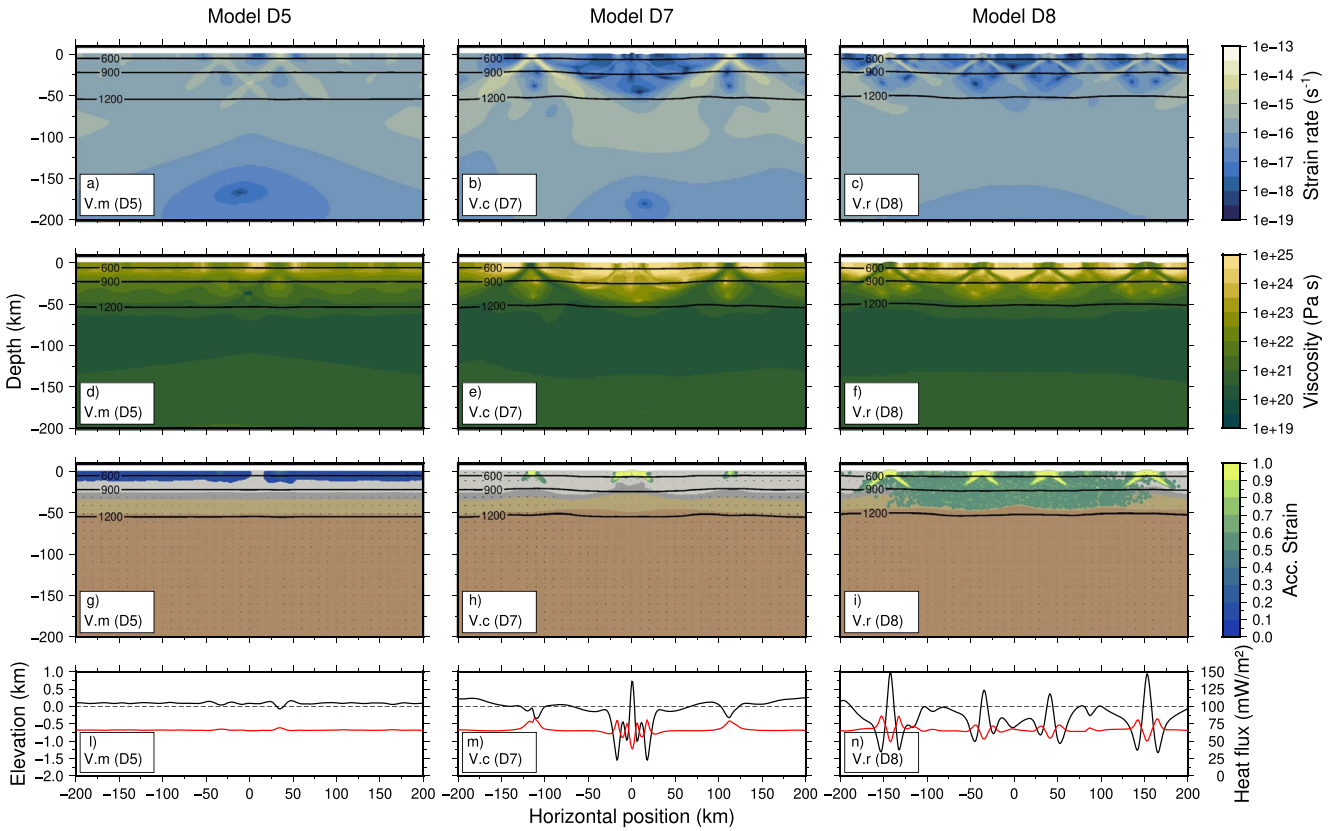

Figure 8. Final distribution of strain rates (first row), viscosities (second row), and composition with accumulated strain (third row) of models with Venus conditions and a wet diabase crustal rheology and dry olivine mantle rheology with a 35 km-thick crust and different methods of localizing initial deformation (i.e., types of weak seeds) at 20 Myr. Left column model D5 with a 6 × 6 km mantle seed (V.m); middle column model D7 with a 6 × 6 km crustal seed (V.c); right column model D8 with random seeding (V.r). Accumulated strain for models D7 and D8 is plotted only if higher than 0.5. Black lines represent 600, 900, and 1200°C isotherms. Background colors are defined by the composition in panels g, h, and i as in Figure 2. Continuous and dashed black lines in panels (l–n) represent the topography and the initial topography, respectively, while red lines represent the heat flux.

with model Q1 in Figures 4d–4f). In addition, the shear bands that develop in the crust at the start of the evolution are characterized by strain rates at least one order of magnitude higher than in model with a wet quartzite and wet anorthite crustal rheology (Figure 7a). The higher strain rates produce a faster strain accumulation in the crust, originating crustal breakup after approximately 9–10 Myr (Figure 7f). However, mantle upwelling is a bit slower, resulting both in a slight smaller final area of melt and a lower melt fraction (maximum 2%) than in model Q1 (compare the dark brown patch in Figure 7f with model Q1 in Figure 4i). Apart from that, the final asymmetric large scale distribution of the accumulated strain is very similar to the one from model Q1 (Figure 7f). This stronger crustal rheology produces larger vertical offset with respect to model Q1 (continuous black and dashed red lines in Figure 7h for models D1 and Q1, respectively). In particular, the maximum height on the left and right side of the rift are approximately 3.2 and 4.7 km, respectively, roughly three times than model Q1. Similarly, the depth of the basin is approximately twice than in model Q1 (5 and 2.5 km for models D1 and Q1, respectively).

Similar to the models with a wet quartzite and wet anorthite rheology for the upper and lower crust, the addition of the surface pressure and the gravitational acceleration of Venus (models D2 and D3, respectively) do not significantly affect the general evolution of the models characterized by a diabase crustal rheology. The only difference is the extent of the melting area, which does not develop in the model including the surface pressure of Venus (model D2), but it is larger in the model with the Venusian gravitational acceleration (model D3). Adding the temperature profile of Venus (model D4) does not result in strain localization, resulting in the absence of mantle upwelling as well as melting.

3.2.2. Venus Models With a 35 km-Thick Crust—Models D5–D8

Using a diabase rheology for the crust has a clear impact on the evolution of the models with surface pressure and temperature, gravity, and lithospheric thickness of Venus, as most models now show clear localization of strain

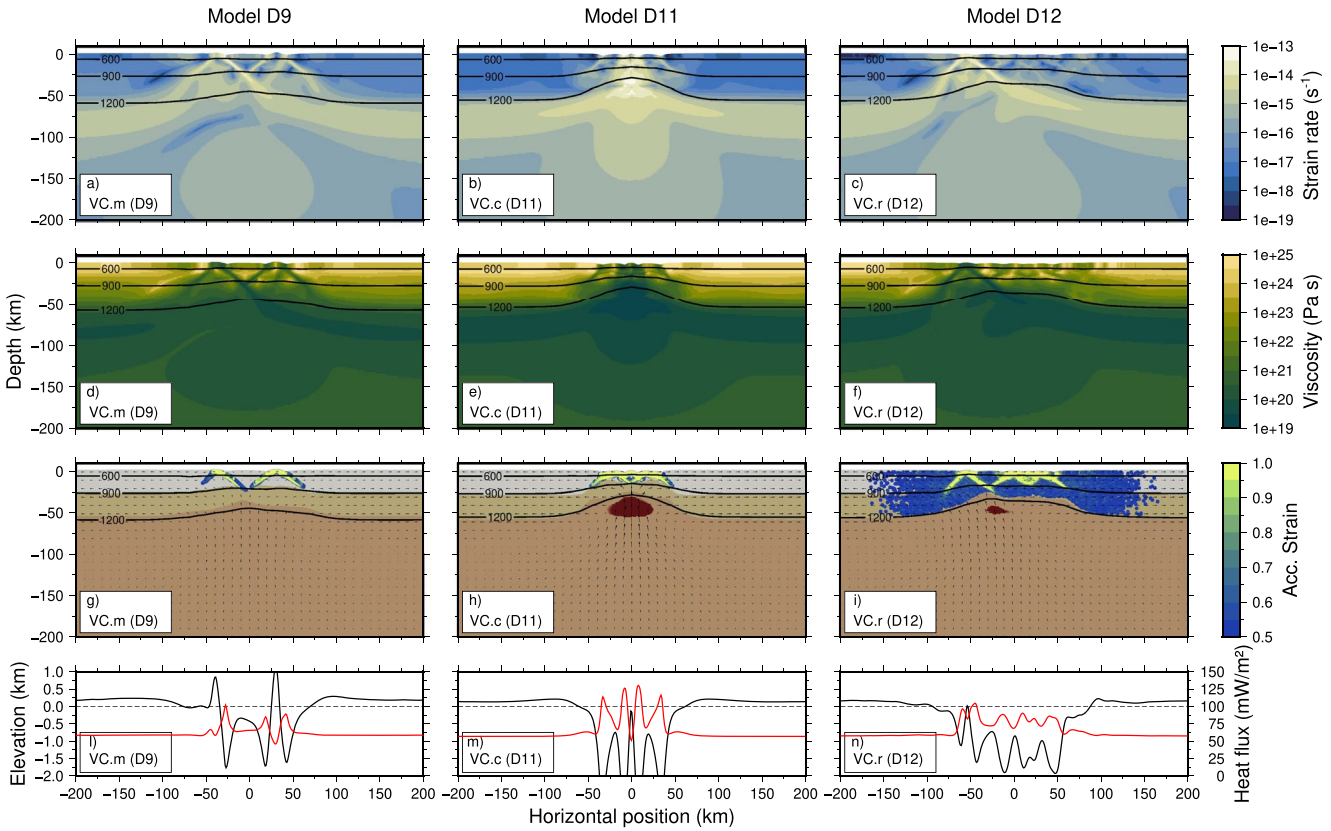

Figure 9. Final distribution of strain rates (first row), viscosities (second row) and composition with accumulated strain (third row) of models with Venus conditions and a wet diabase crustal rheology and dry olivine mantle rheology with a 25 km-thick crust and different methods of localizing initial deformation. Left column model D9 with a 6 × 6 km mantle seed at 20 Myr of model evolution (VC.m); middle column model D11 with a 6 × 6 km crustal seed at 8 Myr (VC.c) and; right column model D12 with random seeding at 10 Myr (VC.r). Note that the accumulated strain is shown only if $\varepsilon_t > 0.5$. Black lines represent 600, 900, and 1200°C isotherms. Background colors are defined by the composition in panels (g–i) as in Figure 2; dark brown indicates melt. Continuous and dashed black lines in panels (l–n) represent the topography and the initial topography, respectively, while red lines represent the heat flux.

in contrast to the lack of strain localization in the corresponding models with a wet quartzite and wet anorthite crustal rheology. In fact, this stronger rheology allows the presence of a brittle layer of approximately 9 km in the upper crust (dashed red line in the strength profile of Venus in Figure 2), similar to the reference terrestrial model with the wet quartzite/wet anorthite crust (model Q1). Consequently, the only Venus model with a 35 km-thick crust that does not show strain localization or deformation in the lithosphere is the model with the mantle seed (model D5 in Figures 8a, 8d, and 8g).

In contrast, the model with 6 × 6 km crustal seed (model D7) results in the development of symmetric shear bands at the beginning of the evolution (point Sr1 in Figure 8b), with a consequent accumulation of strain in the center of the domain (point Sa1 in Figure 8h). The initial shear bands developed in model D7 then slowly became less effective, while new shear bands developed in two areas approximately 100 km from the geometric center of the model domain (points Sr2 in Figure 8b and Movie S5 in Supporting Information S1), causing new accumulation of the strain (points Sa2 in Figure 8h). The repositioning of the shear bands results in a more diffuse deformation in the lithosphere, with a consequent small mantle upwelling that prevents the mantle from melting (Figure 8h).

Similar behavior is observed in the model with random seeding (model D8 in Figures 8c, 8f, and 8i). In the first stages of the evolution, the strain begins to accumulate symmetrically in two areas close to the center of the domain (points Sa1 in Figure 8i). However, with time, new shear bands characterized by the highest strain rates develop toward the boundaries (points Sr1 and Sr2 in Figure 8c and Movie S6 in Supporting Information S1), causing the strain to be accumulated in two new areas (points Sa2 in Figure 8i). Similar to the model with the crustal seed (model D7), this diffuse deformation results only in a small mantle upwelling and does not result in any mantle melting (Figure 8i). The development of shear bands and the localization of the strain in models D6,

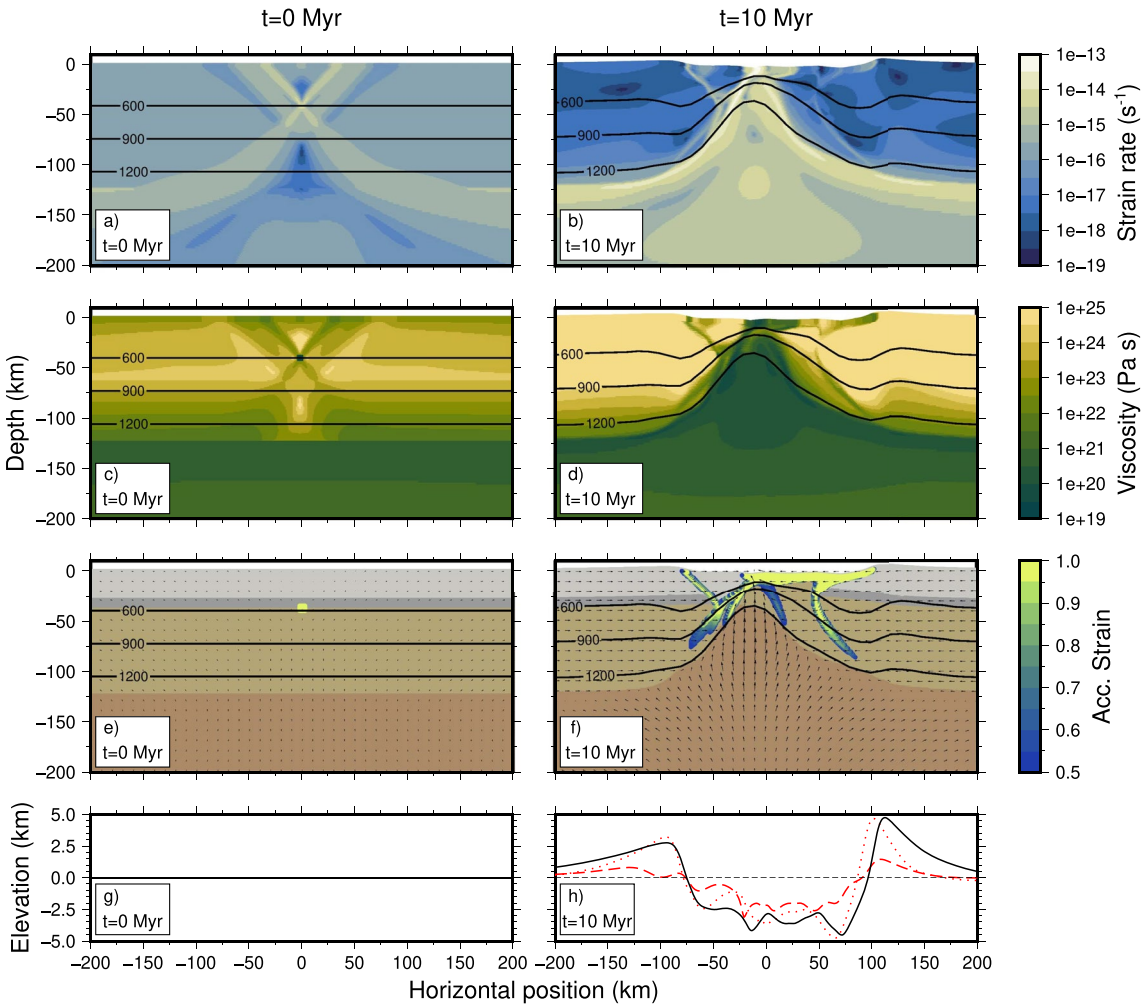

Figure 10. Evolution of strain rates (first row), viscosities (second row), and composition with accumulated strain (third row) of a model with the conditions of the Earth and a dry dunite rheology for the mantle (model DD1) at 0 Myr (left column) and 10 Myr (right column). Note that the accumulated strain is shown only if $\varepsilon_t > 0.5$. Black lines in panels (a–f) represent 600, 900, and 1200°C isotherms. Background colors are defined by the composition in panels e and f as in Figure 2. Continuous and dashed black lines in panels (g and h) represent the topography and the initial topography, respectively; dashed and dotted red lines in panels g and h represent topography of models Q1 and D1, respectively.

D7 and D8 (Figures 8b and 8c) result in higher viscosities in the crust (Figures 8e and 8f) with respect to model D5 (Figure 8d), in which the strain rates are generally higher due to the diffuse deformation pattern (Figure 8a). This behavior is similar to those observed in models characterized by Earth conditions (models Q1 and D1).

The lack of lithospheric deformation of model D5 determines the absence of the development of a topography (continuous black line in Figure 8l). Conversely, the topography in models D7 and D8 is well developed at the end of the evolution (continuous black lines in Figures 8m and 8n) but with lower peaks (maximum 1 km) and shallower basins (maximum 1.5 km) than the terrestrial model D1. In addition, models D7 and D8 show their highest peaks in correspondence of the high strain rates conjugate bands, in the middle of the opening basins, while model D1 has its highest peaks on the sides of the basin. Similarly, the heat flux predicted in model D5 is constant along the whole surface (red line in Figure 8l), while in models D7 and D8 there is a slight variations in correspondence of the conjugate shear bands with respect to the average values in the far-field, with the decrease of approximately 10–20 mW m^{-2} where the highest topography is predicted (red lines in Figures 8m and 8n).

3.2.3. Venus Models With 25 km-Thick Crust—Models D9–D12

Venus models with 25 km-thick crust show more strain localization, regardless of the seed used. More specifically, the model with a mantle seed (model D9) shows typical shear bands characterized by high strain rates (Figure 9a), with the corresponding highly localized strain accumulation pattern (Figure 9g). The rift evolution

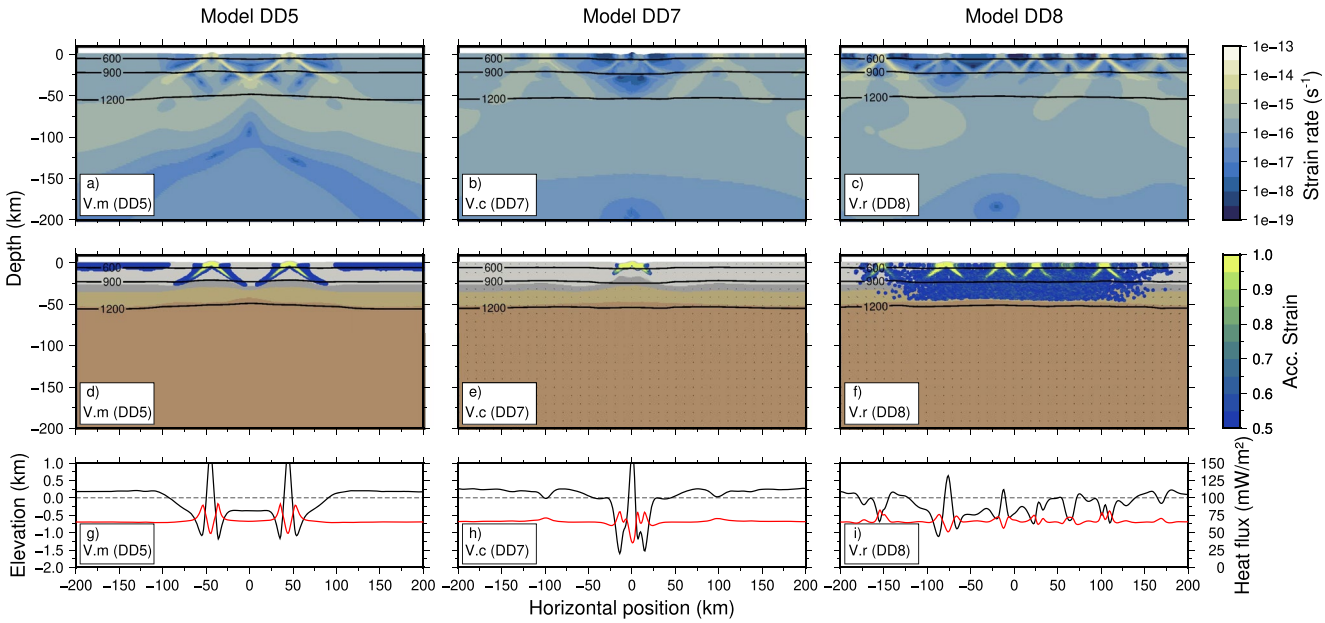

Figure 11. Final distribution of strain rates (first row) and composition with accumulated strain (second row) of models with Venus conditions and a diabase crustal rheology and dry dunite mantle rheology at 20 Myr for different methods of initiating deformation (i.e., types of weak seeds). Left column model DD5 with a 6 × 6 km mantle seed (V.m); middle column model DD7 with a 6 × 6 km crustal seed (V.c); and right column model DD8 with random seeding (V.r). Note that the accumulated strain is shown only if $\varepsilon_t > 0.5$. Black lines represent 600, 900, and 1200°C isotherms. Background colors are defined by the composition in panels (d–f) as in Figure 2. Continuous and dashed black lines in panels g–i represent the topography and the initial topography, respectively, while red lines represent the heat flux.

of this model is slower than that of models with Earth conditions (models Q1 and D1) but nevertheless shows the beginning of asymmetric rifting during the last stages of the model, as revealed by the lower strain rates, the higher viscosities, and the lower accumulated strain on the left portion of the model domain at the end of the evolution (Figures 9a, 9d, and 9g).

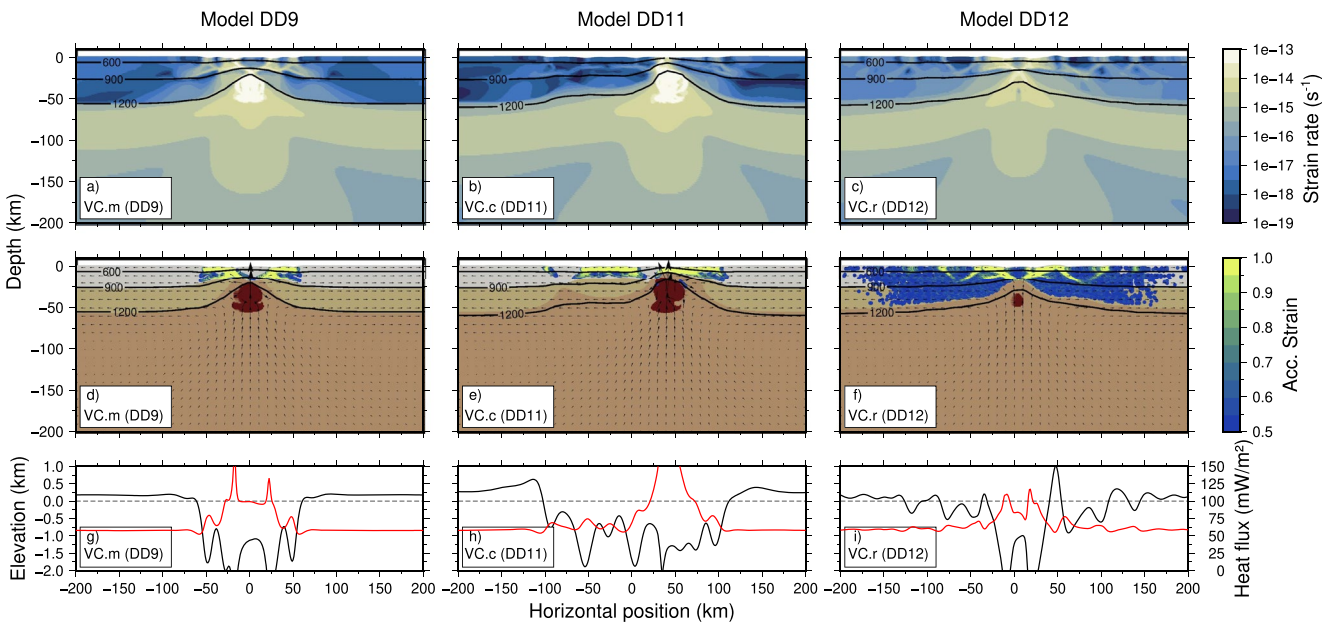

Figure 12. Final distribution of strain rates (first row) and composition with accumulated strain (second row) of models with Venus conditions and a diabase crustal rheology and dry dunite mantle rheology for a 25 km-thick crust for different methods of initiating deformation (i.e., types of weak seeds). Left column model DD9 with a 6 × 6 km mantle seed at 10 Myr (VC.m); middle column model DD11 with a 6 × 6 km crustal seed at 20 Myr (VC.c) and; right column model DD12 with random seeding at 20 Myr (VC.r). Note that the accumulated strain is shown only if $\varepsilon_t > 0.5$. Black lines represent 600, 900, and 1200°C isotherms. Background colors are defined by the composition in panels (d–f) as in Figure 2; dark brown indicates melt. Continuous and dashed black lines in panels (g–i) represent the topography and the initial topography, respectively, while red lines represent the heat flux.

The 6 × 6 km crustal seed model (model D11) has a much faster evolution than both the model with the mantle seed and all of the models with the 35 km-thick crust. Note therefore that the last stage presented in Figures 9b, 9e, and 9h is at 8 Myr instead of the usual 20 Myr. In this model, there is no development of new shear bands toward the borders (Figure 9b) and the strain accumulates only in the central portion of the domain (Figure 9h). This results in a fast symmetric evolution of the model, with early mantle upwelling and melting in the mantle after just 5.5 Myr model time, with maximum melt fraction of 7% (dark brown in Figure 9h).

Similar to model D11, the model with the random seed (model D12) shows a faster evolution with respect to the previous models and the last stage is depicted at 10 Myr (Figures 9c, 9f, and 9i). However, in this model the rift evolution is strongly asymmetric, similar to that observed in models with Earth conditions (models Q1–Q4). In fact, new shear bands develop toward the left (points Sr1 and Sr2 in Figure 9c and Movie S7 in Supporting Information S1), resulting in low viscosities and in an asymmetric upwelling of the mantle (Figures 9f and 9i, respectively). The initial shear bands can be identified by the strain accumulated in the middle of the domain (point Sa1 in Figure 9i), where there are no high strain rates at the end of the evolution (point Sr1 in Figure 9c). Similarly, the final area of high strain rates can be clearly identified (point Sr2 in Figure 9c) and it corresponds to the accumulation of strain on the left of the domain (point Sa2 in Figure 9i). Although this model evolves quickly, the behavior of the shear bands spreads out the accumulation of the strain (Figure 9i), delaying the mantle upwelling with respect to model D11 and consequently melting only occurs after 10 Myr model time and the maximum melt fraction is 1% (dark brown in Figure 9i).

The higher lithospheric deformation observed in model D9 with respect to the 35 km-crust model D5 determines a clear topography at the end of the evolution (continuous black line in Figure 9l). In addition, this is the only model with a 25 km crust that shows some peaks above the initial topography, while models D11 and D12 are characterized by wider and deeper basins than models D7 and D8 (with a 35 km crust) and there are no peaks above 0 km (continuous black lines in Figures 9m and 9n). The heat fluxes predicted by all of these models (red lines in Figures 9l–9n) show clear differences with respect to models D5, D7, and D8 (red lines in Figures 8l–8n). In fact, in all of these models there is an evident increase of heat flux in correspondence of the opening basins, with values up to 70–80 mW m^{-2} higher than in the far-field (red lines in Figures 9l–9n). This increase is more evident in models D11 and D12 that are characterized by melting but can be observed also in model D9 that does not have any melting and has an evolution more similar to models D7 and D8.

3.3. Models With a Diabase Rheology in the Crust and Dry Dunite in the Mantle

In the following models, we use a dry dunite rheology for the mantle of Venus in addition to the diabase rheology of the crust (e.g., Byrne et al., 2021; Ghail, 2015).

3.3.1. Earth Model and Effects of Venusian Surface Conditions: Pressure, Gravitational Acceleration, and Temperature—Models DD1–DD4

The dunite mantle rheology model with the conditions of the Earth (model DD1) shows an evolution comparable to that observed for the corresponding models with weaker rheologies for the mantle and for the crust, with an asymmetric final rift geometry. The initial strain rates in the crust are lower than those in the model with a dry olivine rheology (model D1) but shear bands in the mantle are less diffuse (Figure 10a). At the same time, the viscosities are higher in the entire lithosphere (Figures 10c and 10d), which result in a slower rift evolution with respect to model D1 and there is no occurrence of crustal breakup after 10 Myr (Figure 10f). However, the final topography is almost the same than the one predicted in model D1, with both the same maximum heights on the sides of the rift and the same depth of the basin (continuous black and dotted red lines in Figure 10h for models DD1 and D1, respectively). In contrast to the models with weaker rheologies for the mantle (model D1) and for the crust (model Q1), there is no melting at the end of the evolution and the accumulated strain is more localized along shear bands (Figure 10f).

The addition of the surface pressure and the gravitational acceleration of Venus (models DD2 and DD3, respectively) do not have any significant effects on the evolution. In fact, unlike the diabase and dry olivine models (models D1, D2, and D3), in which surface pressure and gravitational acceleration had an impact on the extent of the melting area, none of these models develop conditions compatible with mantle melting. Adding the temper-

ature profile of Venus (model DD4) results in a lack of development of shear bands, similar to model D4. As a consequence, there is no strain localization, mantle upwelling, or melting.

3.3.2. Venus Models With 35 km-Thick Crust—Models DD5-DD8

The stronger dry dunite rheology used for the mantle produces an increase of approximately 20 MPa in the stress profile of the lithospheric mantle, but the lithosphere continues to deform by viscous creep, without the presence of a brittle layer (dark brown line in Figure 2). However, models with conditions of Venus and a 35 km-thick crust show a similar evolution to what we observed in the corresponding models with a dry olivine rheology for the mantle (models D5-D8). Nonetheless, the timing of the rifting is different depending on the type of weak seed employed. The model with the mantle seed (model DD5) has shear bands in the upper part of the crust, with a consequent faster localization of strain (Figures 11a and 11d, respectively) with respect to the corresponding dry olivine mantle model (model D5). Nonetheless, there is only a slight mantle upwelling after 20 Myr of evolution and no melt is produced (Figure 11d).

The model with the 6×6 km crustal seed (model DD7) evolves similarly to the corresponding dry olivine model (model D7) and after 20 Myr the strain accumulates in the center of the domain, with a slight mantle upwelling and no mantle melting (Figure 11e). Even if there is no clear evidence of the development of new shear bands toward the boundaries as observed in model D7, the beginning of this kind of behavior can be seen in Figure 11b. In fact, shear bands with the higher strain rates at the end of the evolution are in two new areas (points Sr2 in Figure 11b) less centered than the initial location, which can be recognized by the distribution of the accumulated strain (points Sr1 and Sa1 in Figures 11b and 11e, respectively, and Movie S8 in Supporting Information S1).

The evolution of the continental rifting in the model with random seeding (model DD8) is similar to what we observed in the corresponding dry olivine model (model D8). However, the initial shear bands are not symmetric but instead, they are positioned to the left of the center of the domain (point Sr1 in Figure 11c), corresponding to the larger accumulated strain bands (point Sa1 in Figure 11f). Subsequently, new shear bands develop to the right of the center of the domain which result in the localization of strain in two new locations (points Sr2 and Sa2 in Figures 11c and 11f, respectively). The original strain accumulation location then moves toward the left, while the two successive locations move to the right. The position of the final shear bands is indicated by the higher strain rates and the strain accumulation pattern after 20 Myr (points Sr3 and Sa3 in Figures 11c and 11f, respectively and Movie S9 in Supporting Information S1). Similar to model D8, the leap of the shear bands results in more diffusive deformation, allowing a slight mantle upwelling but preventing the melting of the mantle (Figure 11f).

The evolution of the topography in these models is similar to that observed for models D5, D7, and D8. In fact, the topography is well developed at the end of the evolution (continuous black lines in Figures 11g–11i) and is characterized by similar heights (approximately 1 km) and depths (approximately 1.5 km). In the same way, models DD7 and DD8 show their highest peaks in the middle of the opening basins, differently from what observed in model DD1 (compare continuous black lines in Figures 11h and 11i and in Figure 10h, respectively). Similarly, the heat fluxes in correspondence of the rifting show little differences with respect to the far-field, with variations between -20 and 20 mW m^{-2}, with minimum values where the highest topography is predicted (red lines in Figures 11g–11i), as observed in the 35 km-crust models D5, D7, and D8.

3.3.3. Venus Models With 25 km-Thick Crust—Models DD9-DD12

Using a 25 km-thick crust (model DD9-DD12) amplifies the differences in the timing of rift evolution with respect to the corresponding models with dry olivine mantle rheology (models D9-D12). In particular, the evolution of the model with the mantle seed is much faster (model DD9 with respect to model D9). More specifically, model DD9 shows a very fast symmetric evolution of the rifting with the shear bands located in the central portion of the domain (Figure 12a). This results in very localized accumulated strain and a faster upwelling of the mantle, with consequent melting after just 6.5 Myr and a higher melt fraction (maximum 7%: dark brown in Figure 12d). Therefore, the last stage presented in Figures 12a and 12d is at 10 Myr instead of the usual 20 Myr.

Conversely, the evolution of the rifting in case of a crustal and random seeds is clearly slower (models DD10–DD12 compared to models D10–D12). In fact, the rifting in the model with a 6×6 km crustal seed (model DD11) evolves slower than model D11 and its evolution is asymmetric. However, the evolution of the rifting during the initial 10 Myr is symmetric, with the localization and the accumulation of the strain in the middle of the domain (point Sa1 in Figure 12e). In time, new shear bands with the highest strain rates develop on the right of the domain

(point Sr2 and Sa2 in Figures 12b and 12e, respectively, and Movie S10 in Supporting Information S1), resulting in a final asymmetric rift. This behavior of the strain localization could be the reason why the mantle upwelling is delayed compared to model D11, resulting in mantle melting after 15.5 Myr with a melt fraction of 2% (dark brown in Figure 12e).

Similarly, the model with the random seed (model DD12) is slower compared to model D12, with mantle melting occurring after 20 Myr and a maximum melt fraction of 2% (dark brown in Figure 12f). In addition, the evolution of the rifting in this model is strongly symmetric with shear bands and localization of the strain in the center of the domain, different from what we observed in model D12. In contrast to models with mantle and crustal seeds, some minor shear bands with consequent strain localization are observed toward the borders (Figures 12c and 12f, respectively), but the main area of deformation does not move away from the center.

The evolution of the topography in all of these models is similar to what observed for models D11 and D12. In fact, there is the development of a wide and deep basin, with maximum depths of approximately 2.5 km (continuous black lines in Figures 12g–12i). However, differently from the 35 km-crust models, here models DD11 and DD12 show also peaks up to 0.7–1 km on the sides of the basins (continuous black lines in Figures 12h and 12i). Similarly, the heat fluxes predicted by all of these models show an evident increase in correspondence of the rifting, with maximum values up to 200 mW m^{-2} higher than in the far-field (red lines in Figures 12g–12i). In particular, highest values are observed in models DD11 and DD9, where the melting area is wider than in model DD12 (dark brown in Figures 12d–12f).

4. Discussion

4.1. Comparison With Previous Numerical Models

The evolution of our model without viscous weakening is fully comparable to what has been observed by previous numerical models characterized by low divergent velocities and weak crust (e.g., Beucher & Huismans, 2020; Huismans & Beaumont, 2007; Naliboff & Buiter, 2015). In fact, all of these models show a symmetric evolution of the continental rifting throughout the entire numerical experiment, until the crustal break up. However, plastic weakening is limited almost entirely in the crust, while viscous weakening is fundamental to have strain localization and development of a low-viscosity layer in the lithosphere, with potential consequence on the rifting evolution (Bercovici & Ricard, 2012, 2013; Dannberg et al., 2017). We observed that the introduction of the viscous weakening affects the numerical evolution with the consequent development of an asymmetric rifting. The influence of the weakening and its rate on the symmetry of continental rifting has been already noted by Lavier et al. (2000) and Huismans and Beaumont (2003) and the asymmetric behavior of model Q1 is similar to results obtained by Pérez-Gussinyé et al. (2020) and Richter et al. (2021) that implemented both plastic and viscous weakening. In addition, the asymmetric geometry of continental rifting (as in the Red Sea; e.g., Bosworth, 2015; Youssef, 2015) and passive margins (as in the Atlantic; e.g., Flament et al., 2014; Granot & Dyment, 2015) is well documented. In particular, the asymmetric topography observed in model Q1 recall the topography recorded in correspondence of the Conrad Deep in the northern part of the Red Sea, with similar maximum heights of approximately 1,500 m on the eastern side and between 500 and 1,000 m on the western side (Bosworth, 2015; Ehrhardt & Hübscher, 2015). Therefore, the asymmetric evolution of our models is in agreement with both previous numerical models (e.g., Chenin & Beaumont, 2013; Oliveira et al., 2022; Peron-Pinvidic et al., 2022; Theunissen & Huismans, 2022) and natural observation (e.g., Bosworth, 2015; Ehrhardt & Hübscher, 2015; Youssef, 2015) of continental rifting. Since weakening have been proven to have an impact on the evolution of diverge tectonic settings (e.g., Choi et al., 2013; Lavier et al., 1999, 2000), we made a test changing weakening parameters in order to verify if they can affect significantly the evolution of our system (model R2). We observed few differences in the surface distribution of the faults, as previously observed by Choi et al. (2013), but the general large scale evolution is the same than model Q1 and the topography of the two models show same vertical displacements.

4.2. Effects of Venusian Conditions: Surface Pressure, Gravitational Acceleration, and Temperature

We investigated the impact of the surface pressure, gravitational acceleration, and temperature profile of Venus on the evolution of a continental rift in models with a widely used continental crust rheology of wet quartzite and wet anorthite.

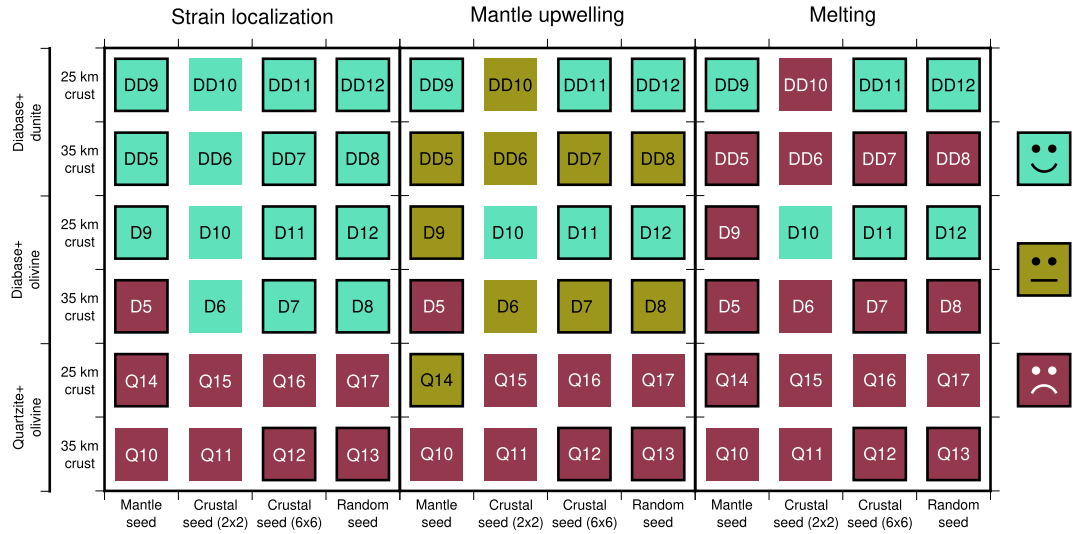

Figure 13. Summary of the results of all of the simulations with Venus conditions. Turquoise squares indicate when strain localization, mantle upwelling, or melting occur. Olive green squares indicate that mantle upwelling occurs partially. Dark red squares indicate a lack of strain localization, mantle upwelling, or melting. We defined the strain localization as the occurrence of shear bands that accumulated at least 0.5 strain. The occurrence of mantle upwelling is defined by both lithospheric thinning and a crustal thinning of at least 50%, while its partial occurrence is identified by lithospheric thinning only. Squares are labeled with the names of the models as in Table 3. Black contours indicates models shown in figures in Section 3.

We observed that the different surface pressure and gravitational acceleration, either used separately or together (models Q2–Q4), do not have any discernible effect on the development of shear bands and the successive localization of strain (Figure 13), resulting in the same asymmetric rifting evolution as in the reference Earth model (model Q1). However, changing these parameters has a slight effect on melting due to the different pressure distribution in the models. For example, the model with surface pressure of Venus (9.3 MPa) but gravitational acceleration of Earth (model Q2) has higher pressures in the entire model domain, resulting in a smaller area with melting conditions. In contrast, the model with surface pressure of Earth and gravitational acceleration of Venus (8.87 m s^{-2}; model Q3) shows lower pressures, with a larger melting domain. Combining the higher Venusian surface pressure with the lower gravitational acceleration (model Q4) results in higher pressures than on Earth in depths shallower than 3.5 km. However, below this depth, the effect of the lower gravitational acceleration prevails and the pressure predicted is lower than on Earth. This results in Venusian pressure up to 150 MPa lower than on Earth between 40 and 50 km depth, with a larger domain under melting conditions with respect to models Q1 and Q2.

Unlike the change in surface pressure and gravitational acceleration, higher Venusian surface temperature and the resulting temperature-depth profile has a major impact on the rift evolution, with the disappearance of the plastic layer. Moreover, Venusian temperatures result in more efficient healing, with a consequent reduction of accumulated strain. Therefore, Venusian temperature conditions combined with a weak crustal rheology (models Q10 to Q17), both in case of a 35 and 25 km-thick crust, act against efficient strain localization, thereby preventing mantle upwelling, melting (Figure 13) and the development of a continental rift. A particular case is model Q9, for which the temperatures at the bottom of the lithosphere are so high that the entire sublithospheric mantle is under melting conditions. However, mantle melting on present-day Venus is hypothesized to occur in case of hot upwelling mantle underlying the major rift systems (e.g., Ghail, 2015) and, therefore, the thermal profile considered for this model is not compatible with Venus.

4.3. Effects of the Lithospheric Structure

Since a crust characterized by wet quartzite and wet anorthite rheologies does not allow for the development of a continental rift despite evidence of rift structures on Venus (e.g., D. B. Campbell et al., 1984; Foster & Nimmo, 1996; Guseva & Ivanov, 2019; Kiefer & Swafford, 2006; Magee & Head, 1995; Masursky et al., 1980;

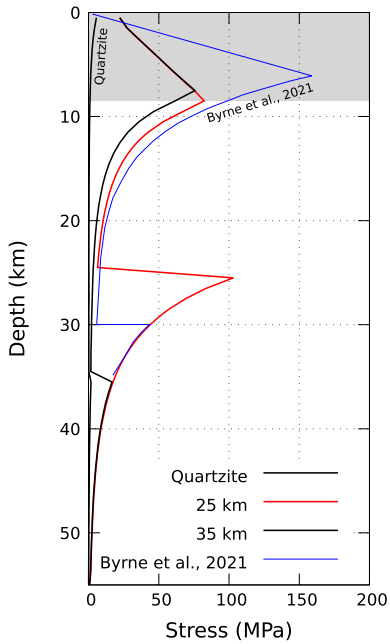

Figure 14. Lithospheric stress profile calculated in the diabase-dunite models for 35 (models from DD5 to DD8) and 25 (models from DD9 to DD12) km-thick crust (continuous red and dashed black lines, respectively) compared to the stress profile from viscous flow models in case of a 30 km-thick crust calculated by Byrne et al. (2021) (dash-dotted blue line). The gray area indicates the maximum portion of the lithosphere characterized by plastic behavior.

Shalygin et al., 2015; Stoddard & Jurdy, 2012), we tested models with a stronger rheology for the whole crust using a diabase flow law (e.g., Byrne et al., 2021; Kohlstedt & Mackwell, 2009; Mackwell et al., 1998). In addition, we tested models with a stronger rheology for the mantle of dry dunite (e.g., Byrne et al., 2021; Ghail, 2015). However, the two different mantle rheologies implemented (dry olivine and dry dunite) produce similar viscosities, in agreement with constraints of Venusian mantle viscosities estimated by previous studies (e.g., Rolf, Steinberger, et al., 2018).

4.3.1. Stress Profiles

The implementation of a stronger crustal rheology in models with the diabase flow law results in a layer characterized by a plastic behavior in the upper crust also under Venus conditions. This behavior occurs both in case of dry olivine (D models) and dry dunite (DD models; gray area in Figure 14) mantle rheology and it is not observed in models with the wet quartzite crustal rheology (continuous black line in Figure 14). The lithospheric stress profiles predicted by the models with a diabase crustal rheology for the crust and dry dunite for the mantle show a good fit with the stress profiles associated with gravitationally inferred mantle motion (for details see the viscous flow modeling by Byrne et al. (2021)) for a 30 km-thick crust model (compare continuous red and dashed black lines with dash-dotted blue line in Figure 14). Differences between our lithospheric stress profiles and the one from Byrne et al. (2021) are observed mainly in the plastic behavior in the shallower portion of the crust. However, these differences are restricted to the shallowest 7–9 km (gray area in Figure 14) and are related to the assumed cohesion and the friction angle of the Venusian crust, which are not well constrained. Nonetheless, maximum crustal yield stress of approximately 80 MPa predicted by models with the diabase rheology for the crust and either a dry olivine or a dry dunite rheology for the mantle (D and DD models, respectively; continuous red and dashed black lines in Figure 14) is in agreement with values calculated for tectonic processes associated to either a plutonic squishy lid or an episodic lid regime (e.g., Armann & Tackley, 2012; Lourenço et al., 2020; Moresi & Solomatov, 1998; Uppalapati et al., 2020). In fact, mobile and stagnant regimes have recently been associated to lower (<30–50 MPa) and higher (>120–160 MPa) surface yield stress, respectively (Lourenço et al., 2020). Previous studies based on the inferred crustal thicknesses of Venus suggested that the episodic lid regime could be more applicable for Venus' evolution than a purely stagnant lid regime (Rolf, Steinberger, et al., 2018), while more recent studies advance the hypothesis that a squishy lid regime could be more suitable to explain the tectonics of Venus (Byrne et al., 2021; Lourenço, 2023; Smrekar et al., 2022). Therefore, the diabase rheology used in our models seems to recreate the surface stress hypothesized for Venus well. However, we want to stress that these values are strongly related to rheological parameters which are poorly known for Venus.

4.3.2. Strain Localization

The different rheological behavior in the crust in the models with a diabase flow law for the crust, and either a dry olivine or a dry dunite for the mantle (models D and DD, respectively), results in the development of up to two orders of magnitude higher strain rates in shear bands in the crust, with a resulting faster strain accumulation. Although this difference does not have big effects in model with Earth conditions (models D1–D3 and DD1–DD3), apart from a slightly slower rifting evolution (model D1 in Figure 7 and model DD1 in Figure 10), major differences are seen in the models with Venus conditions (models D5-12 and DD5-DD12). In fact, Figure 13 shows that the use of a diabase rheology for the crust drastically changes the capacity of the model to localize strain, irrespective of the mantle rheology (compare Q vs. D and DD models of Figure 13).

Considering models with a dry olivine rheology for the mantle (D models), the only model with a diabase crustal rheology that does not show any strain localization is the one with the mantle seed and a 35 km-thick crust (model D5, dark red square in Figure 13). This is because the mantle seed produces low strain rates at the bottom of the crust, resulting in very slow localization of the strain. In addition, high temperatures at the crust-mantle interface determine more efficient healing, with an additional reduction of accumulated strain. In contrast, crustal and

random seeds allow the development of shear bands in a shallower portion of the crust characterized by lower temperatures. This results in less efficient healing and a faster localization of the strain (models D6–D8, turquoise squares in Figure 13). These differences are attenuated in case of 25 km thick crust and, in fact, all models localize strain efficiently (modes D9–D12, turquoise squares in Figure 13). In case of a dry dunite mantle rheology (DD models), all models with either a 35 or a 25 km thick crust produce higher strain rates at the beginning of the numerical simulations. This results in a faster strain localization with respect to D models (models DD5-DD12, turquoise squares in Figure 13), with the development of rift-like faults and structures. Therefore, the evolution of these models is less affected by the choice of weak seed. The necessity to simulate a basaltic crust with a strong diabase flow law to localize the strain and to develop rift-like structures under Venusian conditions is in agreement with the hypothesis regarding the absence of water on Venus that would preclude the formation of extensive felsic crust (I. H. Campbell & Taylor, 1983; Schubert et al., 2001). However, the water content of the interior of Venus remains poorly known, as measurements are available only for the atmosphere, and some authors suggested that the crust involved in the formation of specific tesserae could have felsic composition (Gilmore et al., 2015; Resor et al., 2021).

4.3.3. Mantle Upwelling and Melting

The lack of strain localization in the models with quartzite-anorthite crustal rheology means that neither significant mantle upwelling nor the related melting occurs in these models (models Q10–Q17 in Figure 13). The picture is more complex when looking at models with a diabase crustal rheology. All diabase models with a 35 km-thick crust are characterized by a slight mantle upwelling (models D6–D8 and DD5–DD8; olive green squares in Figure 13), with the exception of the model with a mantle seed and a dry olivine rheology for the mantle (model D5; dark red squares in Figure 13). The lack of mantle upwelling in model D5 is related to its inability to localize the strain and, therefore, to produce crustal thinning. However, the overall evolution of the majority of the 35 km-thick models (models D6–D8 and DD5–DD8) is similar, showing a general symmetric development of high strain rate shear bands localized in the upper crust, followed by a general development of new shear bands toward the boundaries of the model domain. This migration of deformation in the crust suppresses localized mantle upwelling in all of the 35 km-thick crust models (olive green squares in Figure 13) and prevents the development of conditions compatible with mantle melting (dark red squares in Figure 13).

On the contrary, all 25 km-thick diabase crust models show either a partial or a pronounced mantle upwelling, resulting in melting in most of these models. In fact, continental rifting in all of the 25 km-thick crustal diabase models (models D10, D11, D12, DD9, DD11, and DD12) is fast and shows pronounced mantle upwelling and mantle melting within 20 Myr of evolution (turquoise squares in Figure 13), as a result of the better localization of strain and less diffuse crustal deformation compared to the 35 km-thick crust diabase models. The only exceptions are the model with dry olivine mantle rheology and a mantle seed (model D9) and the model with dry dunite and 2×2 km crustal seed (model DD10); these models both produce only very limited mantle upwelling and no melting at all (olive green squares in Figure 13). In particular, the localization of the strain in model D9 is slower because of the highly efficient healing at the crust-mantle interface (as observed for model D5) and, therefore, it needs more time to observe crustal thinning and mantle upwelling. In contrast, the 2×2 km crustal seed in model DD10 allows high strain rates and strain localization in the shallower portion of the crust. However, the smaller size of the seed produces lower strain rates and less strain localization with respect to model DD11, and the strong dry dunite rheology of the mantle reduces the deeper deformation. This results in a slower evolution of this model and a very limited mantle upwelling.

In general, the thickness and rheology of the crust both play a major role on the evolution of rifting on Venus and are more important than the chosen mantle rheology or deformation seed method. More specifically, a rheologically stronger but thinner crust results in mantle melting in most of our models. This is particularly important when considering the recent mounting evidence for volcanic activity inferred for Venus and associated with areas of rifting (e.g., Brossier et al., 2021, 2022; Guseva, 2019; Shalygin et al., 2015; Smrekar et al., 2010). Hence, our models suggest that a thin Venusian crust with a crustal thickness of 25 km or less is more likely in areas of Venus where previous studies inferred recent volcanic activity.

4.4. Comparison With Data From Venus

To assess how well our models capture the rifting process proposed for Venus, here we compare our results to estimated global average surface heat flux values and to observed rift topographies. Since the structures that can

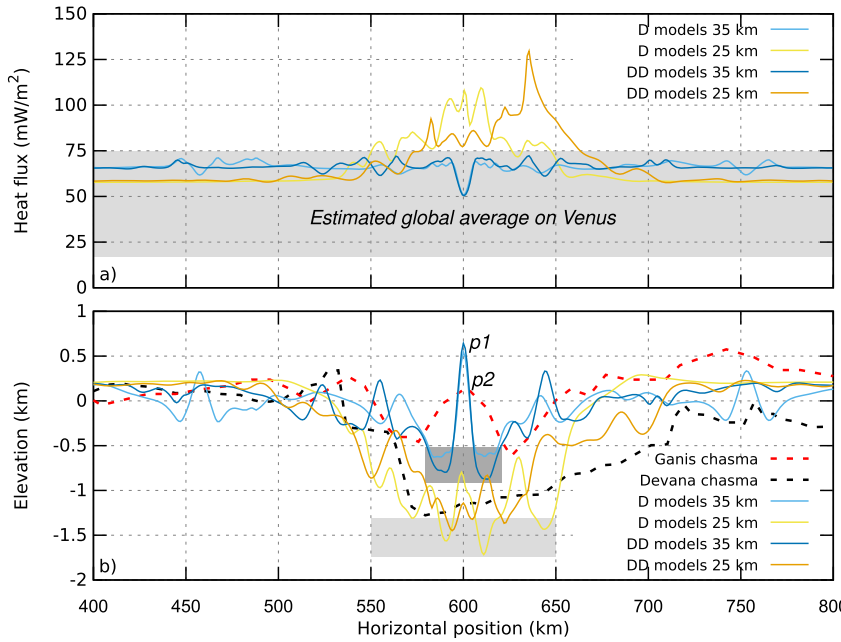

Figure 15. (a) Average heat flux of diabase (D models; light blue and blue lines) and diabase-dunite models (DD models; yellow and orange lines) with a 25 and 35 km-thick crust. The light gray area indicates the estimated global average heat flux estimated for Venus (Gülcher et al., 2020; Smrekar et al., 2022); (b) average topography of diabase (D models; light blue and blue lines) and diabase-dunite models (DD models; yellow and orange lines) with 25 and 35 km-thick crust compared to the average topography of Ganis (Stoddard & Jurdy, 2012) and Devana (Kiefer & Swafford, 2006) Chasmata (dashed red and black lines, respectively). Light and dark gray areas indicate the minimum topography for the 25 and 35 km-thick crust models, respectively. $p1$ indicates the position of the peak topography for the 35 km-thick crust models and $p2$ indicates the peak topography of Ganis chasma.

favor initial localization of the strain are not well known for the lithosphere of Venus, the three different weak zones implemented can be considered equally effective. For this reason, we decided to average surface heat flux and topography for our models with different weak seeds in order to compare them with estimates from Venus (Figures 15a and 15b, respectively). Therefore, we created four composite lines for models with a diabase crust of varying crustal thicknesses and different mantle rheologies.

4.4.1. Heat Flux

Heat fluxes predicted by models with Venus conditions and thickness of the crust of 25 and 35 km show two different trends (Figure 15a). In particular, models with a 35 km-thick diabase crust are characterized by a decrease of the surface heat flux in the center of the domain of approximately 20 mW m^{-2} with respect to the far-field (light blue and blue lines in Figure 15a). In contrast, models with a 25 km-thick diabase crust show a clear increase of the surface heat flux in the proximity of rifting, up to 60 mW m^{-2} (yellow and orange lines in Figure 15a). The higher heat fluxes are related to the upwelling of a large amount of the mantle, resulting in a large area characterized by mantle melting. Since the heat flux is calculated as an average of models with different seeds, the asymmetry displayed by the models with the 25 km-thick crust and a dry dunite mantle rheology (orange line in Figure 15a) is strictly related to asymmetric behavior observed in the model with the crustal seed (model DD11 in Figures 12b and 12e). The maximum values of 110–130 mW m^{-2} predicted by models with 25 km-thick diabase crust (yellow and orange lines in Figure 15a) are comparable with heat fluxes calculated from previous numerical models (e.g., Gülcher et al., 2020) and with maximum heat fluxes of 140 mW m^{-2} estimated in correspondence of fracture belts on coronae on Venus (e.g., O'Rourke & Smrekar, 2018).

Values of 55–60 and 65–70 mW m^{-2} predicted far from the highly deformed area of the rifting by models with 25 and 35 km-thick diabase crust, respectively, are in agreement with the estimates of 20–75 mW m^{-2} for the global average on Venus (light gray area in Figure 15a; Gülcher et al., 2020; Smrekar et al., 2022). However, our models predicted values similar to the maximum estimates for Venus, suggesting that thicker crust are unlikely for the global average of Venus.

4.4.2. Rift Topography

Our results show that a stronger crustal rheology in case of pressure and temperature conditions of the Earth determines more pronounced topography, with both higher peaks on the sides of the rift and deeper basins. Otherwise, different mantle rheology does not impact on the topography. In particular, models with a diabase rheology for the crust and either a dry olivine or a dry dunite rheology for the mantle (models D1 and DD1, respectively) show peaks approximately three times higher and basins twice deeper than the model with the wet quartzite/wet anorthite crust (model Q1). Similarly, Venus conditions in case of diabase rheology for the crust result in a decrease of crustal strength, with consequent lower topography with respect to models characterized by terrestrial conditions. We compare the averaged topography of our models with Venus conditions both with the average topography of Ganis Chasma (Stoddard & Jurdy, 2012) and with a cross-section across the offset zone of Devana Chasma (Kiefer & Swafford, 2006) (dashed red and black lines in Figure 15b, respectively). The topography predicted by the models show two different trends for 25 (yellow and orange lines in Figure 15b) and 35 km-thick (light blue and blue lines in Figure 15b) diabase crust models, while the rheology of the mantle does not significantly change the general trend. Indeed, the averaged minimum topography of both models with a 35 km-thick crust and different rheologies of the mantle show variations of less than 1 km (dark gray area under light blue and blue lines in Figure 15b). In contrast, the models with a 25 km-thick crust have maximum variations of approximately 1.5 km (light gray area under yellow and orange lines in Figure 15b). In addition, the 35 km-thick crust models have a central peak, approximately 1 km higher than the surrounding area (point $p1$ in Figure 15b), while a similar peak is not observed in the 25 km-thick crust models.

The two trends emerging from the models with different crustal thickness each fit well the average topographic features of one of the rifts observed on Venus. In particular, the average topography of the Ganis chasma (dashed red line in Figure 15b) has depressions similar in location and magnitude to those predicted by the 35 km-thick crust models (dark gray area under light blue and blue lines in Figure 15b) while the data also shows a central peak (point $p2$ in Figure 15b) with a similar amplitude to the peak predicted by the 35 km-thick crust models (point $p1$ in Figure 15b). The topography observed across the offset zone of Devana chasma (dashed black line in Figure 15b) is similar to the topography predicted by the 25 km-thick crust models, especially in terms of the amplitude of the central depression and the lack of a central peak that is present in the Ganis chasma (yellow and orange lines in Figure 15b). Therefore, our models capture the first-order topography observed for Venusian rifts, suggesting different crustal thicknesses beneath Ganis and Devana chasma. This is in agreement with the crustal thickness model for Venus by Jiménez-Díaz et al. (2015), which estimated a thicker crust in correspondence of Ganis chasma and the Atla Regio (approximately 30–35 km thick) with respect to Devana chasma in the plains between Beta Regio and Phoebe Regio (approximately 25 km thick).

4.5. Limitations and Future Works

In this work, we mainly focus on crustal variations, including both its rheology and thickness, and we evaluate their effects on the rifting evolution. However, we considered here only crustal thicknesses of 25 and 35 km, while some studies have proposed crustal thickness lower than 25 km down to 8–13 km (e.g., James et al., 2013). As there are so many uncertainties about Venusian material properties and conditions, there are many other parameters that can be investigated in future studies as they could also play major roles in Venusian rift evolution. In particular, initial strength and weakening due to localization of the strain has been proven fundamental for the development and evolution of faults and continental rifting (e.g., Choi et al., 2013; Lavier et al., 1999, 2000) and, therefore, additional analysis considering different weakening and rheological parameters, both viscous and plastic, need to be investigated. In addition, the velocity and duration of extension will have a direct impact on the amount of mantle upwelling and, therefore, on the amount of mantle melting. Similarly, different lithospheric thicknesses, and therefore different thermal profiles, will directly affect the lithospheric strength, thereby increasing or reducing the timescale of rifting evolution. Hence, since the analysis of all these additional parameters is outside the scope of this study, future studies could expand upon the work presented here to include additional crustal and lithospheric thicknesses, thermal profiles, extensional velocities, and weakening/rheological parameters. Even if 3D numerical models allow to simulate more complex and realistic tectonic settings, we here decided to use 2D models to explore in detail specific factors and analyze their impact on the development, evolution and duration of lithospheric-scale tectonic structures. In fact, a better understanding of the dynamics that control rifts on Venus by means of 2D models will allow to better constrain future 3D models.

5. Conclusions

In this work, we investigated the effect of Venusian surface conditions on the development and evolution of a continental rift. We also studied in detail how different crustal and mantle rheologies, crustal thickness, and weak seeds can affect the evolution of the rifting. To assess how well our models correspond to rift observations on Venus, we compared our results, in terms of topography and heat flux, with data and estimates for Venus. We found that although surface pressure and gravitational acceleration of Venus do not majorly affect the evolution of rifting, the increased Venusian surface temperature dramatically changes the lithospheric strength. In fact, the high temperatures of Venus determine the disappearance of a brittle layer in the crust, thus preventing the development of shear bands, strain localization, and the ensuing development of rifting when typical Earth-like rheologies of wet quartzite and wet anorthite are assumed for the crust. Therefore, a stronger rheology, such as diabase, must be taken into account for the crust to observe a thin brittle layer and to ensure localization of strain when modeling the conditions of Venus.

Different combinations of weak seeds and mantle rheologies only partially control the development of rifting in models with Venusian conditions. In particular, a mantle seed results in a faster evolution in case of a stronger mantle (dry dunite), as it is better able to localize the strain at depth. In contrast, crustal and random seeds result in a shallower localization of the strain and the development of the rifting is faster if a dry olivine rheology is used for the mantle.

Conversely, we found that the thickness of the crust has a primary control on the evolution of rifting on Venus. In fact, only models with a 25 km-thick diabase crust show pronounced mantle upwelling that allows for mantle melting. However, it must be noted that our simulations were run for a maximum of 20 Myr, and a longer evolution might also develop conditions favorable for mantle melting for models with a 35 km-thick diabase crust.

The resulting topography of models with crustal thicknesses of 25–35 km and a thin lithosphere fit well with the observed topography of Ganis and Devana Chasmata. In particular, two trends are observed: the 35 km-thick diabase crust models show a topography peak in the center of the domain, similar to the observed topography of Ganis chasma. In contrast, the 25 km-thick diabase crust models show a deeper basin at the rift center, which corresponds to observations of Devana chasma. Therefore, we speculate that a difference in crustal thickness could be the cause of the different rift profiles of Ganis and Devana Chasmata on Venus. In addition, the far field heat fluxes in our models align with highest and latest global average heat flux estimates from previous studies of Venus. Hence, we hypothesize that a global average crust thicker than 35 km is unlikely for Venus.

Data Availability Statement

The numerical code FALCON used in this work together with its complete description and with the results of the benchmarks performed to test the features implemented in the code can be found on the Zenodo online open access repository Regorda (2022). In addition, the same repository provides the input files with properties of the materials and parameters used in this work. The complete data set with the output files in Paraview format (vtu) of all of the models tested in this work can be found on the Zenodo online open access repository Regorda et al. (2022).

Acknowledgments
AR acknowledges the Department of Earth Science of the University of Milan for allowing him to undertake this study while working on other projects. IvZ acknowledges the financial support and endorsement from the DLR Management Board Young Research Group Leader Program and the Executive Board Member for Space Research and Technology. We want to thank two anonymous reviewers, T. Rolf and the Editor L. Montési, for useful comments and suggestions that helped improve this manuscript. All the figures were created with the Generic Mapping Tool (GMT) plotting software (Wessel & Smith, 1998, 2001) using scientific color maps designed by Crameri (2018b), Crameri (2018a), and Crameri et al. (2020).

References

Adams, A. C., Stegman, D. R., Smrekar, S. E., & Tackley, P. J. (2022). Regional-scale lithospheric recycling on Venus via peel-back delamination. *Journal of Geophysical Research: Planets*, *127*(10), e2022JE007460. https://doi.org/10.1029/2022JE007460

Aitta, A. (2012). Venus' internal structure, temperature and core composition. *Icarus*, *218*(2), 967–974. https://doi.org/10.1016/j.icarus.2012.01.007

Alejano, L. R., & Bobet, A. (2012). Drucker-Prager criterion. *Rock Mechanics and Rock Engineering*, *45*(6), 995–999. https://doi.org/10.1007/s00603-012-0278-2

Allken, V., Huismans, R. S., & Thieulot, C. (2011). Three-dimensional numerical modeling of upper crustal extensional systems. *Journal of Geophysical Research*, *116*(10), 1–15. https://doi.org/10.1029/2011JB008319

Amestoy, P. R., Duff, I. S., L'Excellent, J.-Y., & Koster, J. (2001). A fully asynchronous multifrontal solver using distributed dynamic scheduling. *Society for Industrial and Applied Mathematics*, *23*(1), 15–41. https://doi.org/10.1137/s0895479899358194

Amestoy, P. R., Guermouche, A., L'Excellent, J.-Y., & S, P. (2006). Hybrid scheduling for the parallel solution of linear systems. *Parallel Computing*, *32*(2), 136–156. https://doi.org/10.1016/j.parco.2005.07.004

Anderson, J. (1995). *Computational fluid dynamics*. McGraw-Hill.

Anderson, F. S., & Smrekar, S. E. (2006). Global mapping of crustal and lithospheric thickness on Venus. *Journal of Geophysical Research*, *111*(E8), E08006. https://doi.org/10.1029/2004JE002395

Andrés-Martínez, M., Pérez-Gussinyé, M., Armitage, J., & Morgan, J. P. (2019). Thermomechanical implications of sediment transport for the architecture and evolution of continental rifts and margins. *Tectonics*, *38*(2), 641–665. https://doi.org/10.1029/2018TC005346

Andrews, E. R., & Billen, M. I. (2009). Rheologic controls on the dynamics of slab detachment. *Tectonophysics*, *464*(1), 60–69. https://doi.org/10.1016/j.tecto.2007.09.004

Armann, M., & Tackley, P. J. (2012). Simulating the thermochemical magmatic and tectonic evolution of Venus's mantle and lithosphere: Two-dimensional models. *Journal of Geophysical Research*, *117*(E12), E12003. https://doi.org/10.1029/2012JE004231

Arredondo, K. M., & Billen, M. I. (2016). The effects of phase transitions and compositional layering in two-dimensional kinematic models of subduction. *Journal of Geodynamics*, *100*, 159–174. https://doi.org/10.1016/j.jog.2016.05.009

Auzemery, A., Willingshofer, E., Yamato, P., Duretz, T., & Sokoutis, D. (2020). Strain localization mechanisms for subduction initiation at passive margins. *Global and Planetary Change*, *195*, 103323. https://doi.org/10.1016/j.gloplacha.2020.103323

Babeyko, A. Y., & Sobolev, S. V. (2005). Quantifying different modes of the late Cenozoic shortening in the central Andes. *Geology*, *33*(8), 621–624. https://doi.org/10.1130/G21126.1

Balázs, A., Maţenco, L., Granjeon, D., Alms, K., François, T., & Sztanó, O. (2021). Towards stratigraphic-thermo-mechanical numerical modelling: Integrated analysis of asymmetric extensional basins. *Global and Planetary Change*, *196*, 103386. https://doi.org/10.1016/j.gloplacha.2020.103386

Banerdt, W. B., & Golombek, M. P. (1988). Deformational models of rifting and folding on Venus. *Journal of Geophysical Research*, *93*(B5), 4759–4772. https://doi.org/10.1029/JB093iB05p04759

Basilevsky, A. T., & McGill, G. E. (2007). Surface evolution of Venus. In *Exploring Venus as a terrestrial planet* (pp. 23–43). American Geophysical Union. https://doi.org/10.1029/176GM04

Benešová, N., & Čížková, H. (2012). Geoid and topography of Venus in various thermal convection models. *Geodinamica Acta*, *56*(2), 621–639. https://doi.org/10.1007/s11200-011-0251-7

Beniest, A., Koptev, A., & Burov, E. (2017). Numerical models for continental break-up: Implications for the South Atlantic. *Earth and Planetary Science Letters*, *461*, 176–189. https://doi.org/10.1016/j.epsl.2016.12.034

Bercovici, D., & Ricard, Y. (2012). Mechanisms for the generation of plate tectonics by two-phase grain-damage and pinning. *Physics of the Earth and Planetary Interiors*, *202–203*, 27–55. https://doi.org/10.1016/j.pepi.2012.05.003

Bercovici, D., & Ricard, Y. (2013). Generation of plate tectonics with two-phase grain-damage and pinning: Source-sink model and toroidal flow. *Earth and Planetary Science Letters*, *365*, 275–288. https://doi.org/10.1016/j.epsl.2013.02.002

Beucher, R., & Huismans, R. S. (2020). Morphotectonic evolution of passive margins undergoing active surface processes: Large-scale experiments using numerical models. *Geochemistry, Geophysics, Geosystems*, *21*(5), e2019GC008884. https://doi.org/10.1029/2019GC008884

Billen, M. I., & Hirth, G. (2007). Rheologic controls on slab dynamics. *Geochemistry, Geophysics, Geosystems*, *8*(8), Q08012. https://doi.org/10.1029/2007gc001597

Blankenbach, B., Busse, F., Christensen, U., Cserepes, L., Gunkel, D., Hansen, U., et al. (1989). A benchmark comparison for mantle convection codes. *Geophysical Journal International*, *98*(1), 23–38. https://doi.org/10.1111/j.1365-246X.1989.tb05511.x

Bollino, A., Regorda, A., Sabadini, R., & Marotta, A. M. (2022). From rifting to oceanization in the Gulf of Aden: Insights from 2D numerical models. *Tectonophysics*, *838*, 229483. https://doi.org/10.1016/j.tecto.2022.229483

Borrelli, M. E., O'Rourke, J. G., Smrekar, S. E., & Ostberg, C. M. (2021). A global survey of lithospheric flexure at steep-sided domical volcanoes on Venus reveals intermediate elastic thicknesses. *Journal of Geophysical Research: Planets*, *126*(7), e2020JE006756. https://doi.org/10.1029/2020je006756

Bosworth, W. (2015). Geological evolution of the Red Sea: Historical background, review, and synthesis. In N. M. Rasul & I. C. Stewart (Eds.), *The Red Sea: The formation, morphology, oceanography and environment of a young ocean basin* (pp. 45–78). Springer Berlin Heidelberg. https://doi.org/10.1007/978-3-662-45201-1_3

Braun, J., Thieulot, C., Fullsack, P., DeKool, M., Beaumont, C., & Huismans, R. (2008). DOUAR: A new three-dimensional creeping flow numerical model for the solution of geological problems. *Physics of the Earth and Planetary Interiors*, *171*(1–4), 76–91. https://doi.org/10.1016/j.pepi.2008.05.003

Brossier, J., Gilmore, M. S., & Head, J. W. (2021). Possible recent or current rift-associated volcanism in Ganis Chasma, Venus. In *Paper presented at 52nd Lunar and Planetary Science Conference*.

Brossier, J., Gilmore, M. S., & Head, J. W. (2022). Extended rift-associated volcanism in Ganis Chasma, Venus detected from Magellan radar emissivity. *Geophysical Research Letters*, *49*(15), e2022GL099765. https://doi.org/10.1029/2022GL099765

Brune, S., & Autin, J. (2013). The rift to break-up evolution of the Gulf of Aden: Insights from 3D numerical lithospheric-scale modelling. *Tectonophysics*, *607*, 65–79. https://doi.org/10.1016/j.tecto.2013.06.029

Brune, S., Corti, G., & Ranalli, G. (2017). Controls of inherited lithospheric heterogeneity on rift linkage: Numerical and analog models of interaction between the Kenyan and Ethiopian rifts across the Turkana depression. *Tectonics*, *36*(9), 1767–1786. https://doi.org/10.1002/2017TC004739

Buiter, S. J., & Ellis, S. (2012). SULEC: Benchmarking a new ALE finite-element code. In *EGU General Assembly Conference Abstracts* (Vol. 14, p. 7528).

Burov, E. B. (2011). Rheology and strength of the lithosphere. *Marine and Petroleum Geology*, *28*(8), 1402–1443. https://doi.org/10.1016/j.marpetgeo.2011.05.008

Byrne, P. K., Ghail, R. C., Şengör, A. M. C., James, P. B., Klimczak, C., & Solomon, S. C. (2021). A globally fragmented and mobile lithosphere on Venus. *Proceedings of the National Academy of Sciences*, *118*(26), e2025919118. https://doi.org/10.1073/pnas.2025919118

Campbell, D. B., Head, J. W., Harmon, J. K., & Hine, A. A. (1984). Venus: Volcanism and rift formation in Beta Regio. *Science*, *226*(4671), 167–170. https://doi.org/10.1126/science.226.4671.167

Campbell, I. H., & Taylor, S. R. (1983). No water, no granites - No oceans, no continents. *Geophysical Research Letters*, *10*(11), 1061–1064. https://doi.org/10.1029/GL010i011p01061

Chenin, P., & Beaumont, C. (2013). Influence of offset weak zones on the development of rift basins: Activation and abandonment during continental extension and breakup. *Journal of Geophysical Research: Solid Earth*, *118*(4), 1698–1720. https://doi.org/10.1002/jgrb.50138

Choi, E., Buck, W. R., Lavier, L. L., & Petersen, K. D. (2013). Using core complex geometry to constrain fault strength. *Geophysical Research Letters*, *40*(15), 3863–3867. https://doi.org/10.1002/grl.50732

Chopra, P. N., & Paterson, M. S. (1981). The experimental deformation of dunite. *Tectonophysics*, *78*(1–4), 453–473. https://doi.org/10.1016/0040-1951(81)90024-X

Christensen, U. R., & Yuen, D. A. (1985). Layered convection induced by phase transitions. *Journal of Geophysical Research*, *90*(B12), 10291–10300. https://doi.org/10.1029/jb090ib12p10291

Crameri, F. (2018a). Geodynamic diagnostics, scientific visualisation and StagLab 3.0. *Geoscientific Model Development*, *11*(6), 2541–2562. https://doi.org/10.5194/gmd-11-2541-2018

Crameri, F. (2018b). Scientific colour-maps. *Zenodo*. https://doi.org/10.5281/zenodo.1243862
Crameri, F., Magni, V., Domeier, M., Shephard, G. E., Chotalia, K., Cooper, G., et al. (2020). A transdisciplinary and community-driven database to unravel subduction zone initiation. *Nature Communications*, *11*(1), 3750. https://doi.org/10.1038/s41467-020-17522-9
Crameri, F., Schmeling, H., Golabek, G. J., Duretz, T., Orendt, R., Buiter, S. J. H., et al. (2012). A comparison of numerical surface topography calculations in geodynamic modelling: An evaluation of the 'sticky air' method. *Geophysical Journal International*, *189*(1), 38–54. https://doi.org/10.1111/j.1365-246X.2012.05388.x
Dabrowski, M., Krotkiewski, M., & Schmid, D. W. (2008). MILAMIN: MATLAB-based finite element method solver for large problems. *Geochemistry, Geophysics, Geosystems*, *9*(4), 1–24. https://doi.org/10.1029/2007GC001719
Dannberg, J., Eilon, Z., Faul, U., Gassmöller, R., Moulik, P., & Myhill, R. (2017). The importance of grain size to mantle dynamics and seismological observations. *Geochemistry, Geophysics, Geosystems*, *18*(8), 3034–3061. https://doi.org/10.1002/2017GC006944
Davaille, A., Smrekar, S. E., & Tomlinson, S. (2017). Experimental and observational evidence for plume-induced subduction on Venus. *Nature Geoscience*, *10*(5), 349–355. https://doi.org/10.1038/ngeo2928
Davies, D. R., Davies, J. H., Hassan, O., Morgan, K., & Nithiarasu, P. (2007). Investigations into the applicability of adaptive finite element methods to two-dimensional infinite Prandtl number thermal and thermochemical convection. *Geochemistry, Geophysics, Geosystems*, *8*(5), Q05010. https://doi.org/10.1029/2006GC001470
de Oliveira, M. R., Gil, P. J., & Ghail, R. (2018). A novel orbiter mission concept for Venus with the envision proposal. *Acta Astronautica*, *148*, 260–267. https://doi.org/10.1016/j.actaastro.2018.05.012
Dias, A. E. S., Lavier, L. L., & Hayman, N. W. (2015). Conjugate rifted margins width and asymmetry: The interplay between lithospheric strength and thermomechanical processes. *Journal of Geophysical Research: Solid Earth*, *120*(12), 8672–8700. https://doi.org/10.1002/2015JB012074
Donea, J., & Huerta, A. (2003). *Finite element methods for flow problems* (Vol. 1). Wiley. https://doi.org/10.1017/CBO9781107415324.004
Donea, J., Huerta, A., Ponthot, J.-P., & Rodríguez-Ferran, A. (2004). Arbitrary Lagrangian–Eulerian methods. In *Encyclopedia of computational mechanics (Chapter 14)*. John Wiley & Sons, Ltd. https://doi.org/10.1002/0470091355.ecm009
Duretz, T., de Borst, R., & Yamato, P. (2021). Modeling lithospheric deformation using a compressible visco-elasto-viscoplastic rheology and the effective viscosity approach. *Geochemistry, Geophysics, Geosystems*, *22*(8), e2021GC009675. https://doi.org/10.1029/2021GC009675
Duretz, T., Gerya, T. V., & May, D. A. (2011). Numerical modelling of spontaneous slab breakoff and subsequent topographic response. *Tectonophysics*, *502*(1–2), 244–256. https://doi.org/10.1016/j.tecto.2010.05.024
Ehrhardt, A., & Hübscher, C. (2015). The northern Red Sea in transition from rifting to drifting-lessons learned from ocean deeps. In N. M. Rasul & I. C. Stewart (Eds.), *The Red Sea: The formation, morphology, oceanography and environment of a young ocean basin* (pp. 99–121). Springer Berlin Heidelberg. https://doi.org/10.1007/978-3-662-45201-1_5
Elkins-Tanton, L. T., Smrekar, S. E., Hess, P. C., & Parmentier, E. M. (2007). Volcanism and volatile recycling on a one-plate planet: Applications to Venus. *Journal of Geophysical Research*, *112*(E4), E04S06. https://doi.org/10.1029/2006JE002793
Elman, H., Silvester, D., & Wathen, A. (2014). *Finite elements and fast iterative solvers*. Oxford Science Publications.
Erdős, Z., Huismans, R. S., & van der Beek, P. (2019). Control of increased sedimentation on orogenic fold-and-thrust belt structure – Insights into the evolution of the Western Alps. *Solid Earth*, *10*(2), 391–404. https://doi.org/10.5194/se-10-391-2019
Erdős, Z., Huismans, R. S., van der Beek, P., & Thieulot, C. (2014). Extensional inheritance and surface processes as controlling factors of mountain belt structure. *Journal of Geophysical Research*, *119*(12), 9042–9061. https://doi.org/10.1002/2014JB011408
Esposito, L. W. (1984). Sulfur dioxide: Episodic injection shows evidence for active Venus volcanism. *Science*, *223*(4640), 1072–1074. https://doi.org/10.1126/science.223.4640.1072
Esposito, L. W., Copley, M., Eckert, R., Gates, L., Stewart, A. I. F., & Worden, H. (1988). Sulfur dioxide at the Venus cloud tops, 1978–1986. *Journal of Geophysical Research*, *93*(D5), 5267–5276. https://doi.org/10.1029/JD093iD05p05267
Farangitakis, G. P., Heron, P. J., McCaffrey, K. J., van Hunen, J., & Kalnins, L. M. (2020). The impact of oblique inheritance and changes in relative plate motion on the development of rift-transform systems. *Earth and Planetary Science Letters*, *541*, 116277. https://doi.org/10.1016/j.epsl.2020.116277
Flament, N., Gurnis, M., Williams, S., Seton, M., Skogseid, J., Heine, C., & Dietmar Müller, R. (2014). Topographic asymmetry of the South Atlantic from global models of mantle flow and lithospheric stretching. *Earth and Planetary Science Letters*, *387*, 107–119. https://doi.org/10.1016/j.epsl.2013.11.017
Ford, P. G., & Pettengill, G. H. (1992). Venus topography and kilometer-scale slopes. *Journal of Geophysical Research*, *97*(E8), 13103. https://doi.org/10.1029/92je01085
Foster, A., & Nimmo, F. (1996). Comparisons between the rift systems of east Africa, Earth and Beta Regio, Venus. *Earth and Planetary Science Letters*, *143*(1), 183–195. https://doi.org/10.1016/0012-821X(96)00146-X
Fraters, M. R. T., Bangerth, W., Thieulot, C., Glerum, A. C., & Spakman, W. (2019). Efficient and practical Newton solvers for non-linear Stokes systems in geodynamic problems. *Geophysical Journal International*, *218*(2), 873–894. https://doi.org/10.1093/gji/ggz183
Fuchs, L., & Becker, T. W. (2021). Deformation memory in the lithosphere: A comparison of damage-dependent weakening and grain-size sensitive rheologies. *Journal of Geophysical Research: Solid Earth*, *126*(1), e2020JB020335. https://doi.org/10.1029/2020JB020335
Fullsack, P. (1995). An arbitrary Lagrangian-Eulerian formulation for creeping flows and its application in tectonic models. *Geophysical Journal International*, *120*(1), 1–23. https://doi.org/10.1111/j.1365-246X.1995.tb05908.x
Gassmöller, R., Dannberg, J., Bangerth, W., Heister, T., & Myhill, R. (2020). On formulations of compressible mantle convection. *Geophysical Journal International*, *221*(2), 1264–1280. https://doi.org/10.1093/gji/ggaa078
Gerya, T. V. (2010). *Introduction to numerical geodynamic modelling*. Cambridge University Press.
Gerya, T. V. (2013). Three-dimensional thermomechanical modeling of oceanic spreading initiation and evolution. *Physics of the Earth and Planetary Interiors*, *214*, 35–52. https://doi.org/10.1016/j.pepi.2012.10.007
Gerya, T. V. (2014). Plume-induced crustal convection: 3D thermomechanical model and implications for the origin of novae and coronae on Venus. *Earth and Planetary Science Letters*, *391*, 183–192. https://doi.org/10.1016/j.epsl.2014.02.005
Gerya, T. V., Stöckhert, B., & Perchuk, A. L. (2002). Exhumation of high-pressure metamorphic rocks in a subduction channel: A numerical simulation. *Tectonics*, *21*(6), 1–15. https://doi.org/10.1029/2002TC001406
Gerya, T. V., & Yuen, D. A. (2003). Characteristics-based marker-in-cell method with conservative finite-differences schemes for modeling geological flows with strongly variable transport properties. *Physics of the Earth and Planetary Interiors*, *140*(4), 293–318. https://doi.org/10.1016/j.pepi.2003.09.006
Gerya, T. V., & Yuen, D. A. (2007). Robust characteristics method for modelling multiphase visco-elasto-plastic thermo-mechanical problems. *Physics of the Earth and Planetary Interiors*, *163*(1–4), 83–105. https://doi.org/10.1016/j.pepi.2007.04.015
Gerya, T. V., Yuen, D. A., & Maresch, W. V. (2004). Thermomechanical modelling of slab detachment. *Earth and Planetary Science Letters*, *226*(1–2), 101–116. https://doi.org/10.1016/j.epsl.2004.07.022

Ghail, R. (2015). Rheological and petrological implications for a stagnant lid regime on Venus. *Planetary and Space Science*, *113–114*, 2–9. https://doi.org/10.1016/j.pss.2015.02.005
Ghail, R., Wilson, C. F., & Widemann, T. (2016). EnVision M5 Venus orbiter proposal: Opportunities and challenges. In *AAS/Division for Planetary Sciences Meeting Abstracts* (Vol. 48, pp. 216–308).
Gilmore, M. S., Mueller, N., & Helbert, J. (2015). Virtis emissivity of Alpha Regio, Venus, with implications for tessera composition. *Icarus*, *254*, 350–361. https://doi.org/10.1016/j.icarus.2015.04.008
Glerum, A., Thieulot, C., Fraters, M., Blom, C., & Spakman, W. (2018). Nonlinear viscoplasticity in ASPECT: Benchmarking and applications to subduction. *Solid Earth*, *9*(2), 267–294. https://doi.org/10.5194/se-9-267-2018
Graff, J., Ernst, R., & Samson, C. (2018). Evidence for triple-junction rifting focussed on local magmatic centres along Parga Chasma, Venus. *Icarus*, *306*, 122–138. https://doi.org/10.1016/j.icarus.2018.02.010
Granot, R., & Dyment, J. (2015). The cretaceous opening of the South Atlantic Ocean. *Earth and Planetary Science Letters*, *414*, 156–163. https://doi.org/10.1016/j.epsl.2015.01.015
Grimm, R. E. (1994a). The deep structure of Venusian plateau highlands. *Icarus*, *112*(1), 89–103. https://doi.org/10.1006/icar.1994.1171
Grimm, R. E. (1994b). Recent deformation rates on Venus. *Journal of Geophysical Research*, *99*(E11), 23163–23171. https://doi.org/10.1029/94je02196
Gudkova, T. V., & Zharkov, V. N. (2020). Models of the internal structure of the Earth-like Venus. *Solar System Research*, *54*(1), 20–27. https://doi.org/10.1134/S0038094620010049
Gülcher, A. J. P., Gerya, T. V., Montési, L. G. J., & Munch, J. (2020). Corona structures driven by plume–lithosphere interactions and evidence for ongoing plume activity on Venus. *Nature Geoscience*, *13*(8), 547–554. https://doi.org/10.1038/s41561-020-0606-1
Guseva, E. N. (2016). Classification of the rift zones of Venus: Rift valleys and graben belts. *Solar System Research*, *50*(3), 184–196. https://doi.org/10.1134/S0038094616030023
Guseva, E. N. (2019). Spatial and genetic relationships of groove belts, rift zones, and lobate plains on Venus. *Solar System Research*, *53*(3), 151–160. https://doi.org/10.1134/S0038094619020035
Guseva, E. N., & Ivanov, M. A. (2019). Regional geologic and morphologic characterization of rift zones on Venus. *Solar System Research*, *53*(4), 233–244. https://doi.org/10.1134/S003809461904004X
Harris, L. B., & Bédard, J. H. (2015). Interactions between continent-like 'drift', rifting and mantle flow on Venus: Gravity interpretations and Earth analogues. In *Volcanism and tectonism across the inner solar system*. Geological Society of London. https://doi.org/10.1144/SP401.9
Hirth, G., & Kohlstedt, D. (2003). Rheology of the upper mantle and the mantle wedge: A view from the experimentalists. *Geophysical Monograph Series*, *138*, 83–105. https://doi.org/10.1029/138GM06
Huang, J., Yang, A., & Zhong, S. (2013). Constraints of the topography, gravity and volcanism on Venusian mantle dynamics and generation of plate tectonics. *Earth and Planetary Science Letters*, *362*, 207–214. https://doi.org/10.1016/j.epsl.2012.11.051
Hughes, T., & Brooks, A. (1982). A theoretical framework for Petrov-Galerkin methods with discontinuous weighting functions: Application to the streamline-upwind procedure. *Finite Elements in Fluids*, *4*, 47–65.
Huismans, R. S., & Beaumont, C. (2003). Symmetric and asymmetric lithospheric extension: Relative effects of frictional-plastic and viscous strain softening. *Journal of Geophysical Research*, *108*(B10), 1–22. https://doi.org/10.1029/2002JB002026
Huismans, R. S., & Beaumont, C. (2007). Roles of lithospheric strain softening and heterogeneity in determining the geometry of rifts and continental margins. In *Imaging, mapping and modelling continental lithosphere extension and breakup*. Geological Society of London. https://doi.org/10.1144/SP282.6
Huismans, R. S., Buiter, S. J. H., & Beaumont, C. (2005). Effect of plastic-viscous layering and strain softening on mode selection during lithospheric extension. *Journal of Geophysical Research*, *110*(B2), 1–17. https://doi.org/10.1029/2004JB003114
Ivanov, M. A., & Head, J. W. (2011). Global geological map of Venus. *Planetary and Space Science*, *59*(13), 1559–1600. https://doi.org/10.1016/j.pss.2011.07.008
James, P. B., Zuber, M. T., & Phillips, R. J. (2013). Crustal thickness and support of topography on Venus. *Journal of Geophysical Research: Planets*, *118*(4), 859–875. https://doi.org/10.1029/2012JE004237
Jiménez-Díaz, A., Ruiz, J., Kirby, J. F., Romeo, I., Tejero, R., & Capote, R. (2015). Lithospheric structure of Venus from gravity and topography. *Icarus*, *260*, 215–231. https://doi.org/10.1016/j.icarus.2015.07.020
Jourdon, A., Le Pourhiet, L., Mouthereau, F., & May, D. (2020). Modes of propagation of continental breakup and associated oblique rift structures. *Journal of Geophysical Research: Solid Earth*, *125*(9), e2020JB019906. https://doi.org/10.1029/2020JB019906
Karato, S.-I. (2008). *Deformation of Earth materials - An introduction to the rheology of solid Earth*. Cambridge University Press. https://doi.org/10.1017/cbo9780511804892
Katz, R. F., Spiegelman, M., & Langmuir, C. H. (2003). A new parameterization of hydrous mantle melting. *Geochemistry, Geophysics, Geosystems*, *4*(9), 1–19. https://doi.org/10.1029/2002GC000433
Kaus, B. J. P., Mühlhaus, H., & May, D. A. (2010). A stabilization algorithm for geodynamic numerical simulations with a free surface. *Physics of the Earth and Planetary Interiors*, *181*(1–2), 12–20. https://doi.org/10.1016/j.pepi.2010.04.007
Kelley, K. A., Plank, T., Newman, S., Stolper, E. M., Grove, T. L., Parman, S., & Hauri, E. H. (2010). Mantle melting as a function of water content beneath the Mariana Arc. *Journal of Petrology*, *51*(8), 1711–1738. https://doi.org/10.1093/petrology/egq036
Kiefer, W. S., & Peterson, K. (2003). Mantle and crustal structure in Phoebe Regio and Devana Chasma, Venus. *Geophysical Research Letters*, *30*(1), 5-1–5-4. https://doi.org/10.1029/2002GL015762
Kiefer, W. S., & Swafford, L. C. (2004). Rift system architecture on Venus. In *Lunar and Planetary Science Conference* (p. 1607).
Kiefer, W. S., & Swafford, L. C. (2006). Topographic analysis of Devana Chasma, Venus: Implications for rift system segmentation and propagation. *Journal of Structural Geology*, *28*(12), 2144–2155. https://doi.org/10.1016/j.jsg.2005.12.002
King, S., Raefsky, A., & Hager, B. (1990). ConMan: Vectorizing a finite element code for incompressible two-dimensional convection in the Earth's mantle. *Physics of the Earth and Planetary Interiors*, *59*(3), 195–207. https://doi.org/10.1016/0031-9201(90)90225-M
Kohlstedt, D. L., & Mackwell, S. J. (2009). Strength and deformation of planetary lithospheres. In T. R. Watters & R. A. Schultz (Eds.), *Planetary tectonics* (pp. 397–456). Cambridge University Press. https://doi.org/10.1017/CBO9780511691645.010
Korchinski, M., Teyssier, C., Rey, P. F., Whitney, D. L., & Mondy, L. (2021). Single-phase vs two-phase rifting: Numerical perspectives on the accommodation of extension during continental break-up. *Marine and Petroleum Geology*, *123*, 104715. https://doi.org/10.1016/j.marpetgeo.2020.104715
Korenaga, J. (2013). Initiation and evolution of plate tectonics on Earth: Theories and observations. *Annual Review of Earth and Planetary Sciences*, *41*(1), 117–151. https://doi.org/10.1146/annurev-earth-050212-124208
Langmuir, C. H., Bézos, A., Escrig, S., & Parman, S. W. (2006). Chemical systematics and hydrous melting of the mantle in back-arc basins. *Geophysical Monograph Series*, *166*, 87–146. https://doi.org/10.1029/166GM07

Lavier, L. L., Buck, W. R., & Poliakov, A. N. B. (2000). Factors controlling normal fault offset in an ideal brittle layer. *Journal of Geophysical Research*, *105*(B10), 23431–23442. https://doi.org/10.1029/2000JB900108

Lavier, L. L., Roger Buck, W., & Poliakov, A. N. B. (1999). Self-consistent rolling-hinge model for the evolution of large-offset low-angle normal faults. *Geology*, *27*(12), 1127–1130. https://doi.org/10.1130/0091-7613(1999)027⟨1127:SCRHMF⟩2.3.CO;2

Leng, W., & Zhong, S. (2011). Implementation and application of adaptive mesh refinement for thermochemical mantle convection studies. *Geochemistry, Geophysics, Geosystems*, *12*(4), Q04006. https://doi.org/10.1029/2010GC003425

Le Pourhiet, L., Burov, E., & Moretti, I. (2004). Rifting through a stack of inhomogeneous thrusts (the dipping pie concept). *Tectonics*, *23*(4), TC4005. https://doi.org/10.1029/2003TC001584

Le Pourhiet, L., May, D. A., Huille, L., Watremez, L., & Leroy, L. (2017). A genetic link between transform and hyper-extended margins. *Earth and Planetary Science Letters*, *465*, 184–192. https://doi.org/10.1016/j.epsl.2017.02.043

Liao, J., Gerya, T., & Wang, Q. (2013). Layered structure of the lithospheric mantle changes dynamics of craton extension. *Geophysical Research Letters*, *40*(22), 5861–5866. https://doi.org/10.1002/2013GL058081

Lourenço, D. L. (2023). Estranged planetary twins. *Nature Geoscience*, *16*(1), 2–3. https://doi.org/10.1038/s41561-022-01104-z

Lourenço, D. L., Rozel, A. B., Ballmer, M. D., & Tackley, P. J. (2020). Plutonic-squishy lid: A new global tectonic regime generated by intrusive magmatism on Earth-like planets. *Geochemistry, Geophysics, Geosystems*, *21*(4), e2019GC008756. https://doi.org/10.1029/2019GC008756

Mackwell, S. J., Zimmerman, M. E., & Kohlstedt, D. L. (1998). High-temperature deformation of dry diabase with application to tectonics on Venus. *Journal of Geophysical Research*, *103*(B1), 975–984. https://doi.org/10.1029/97JB02671

Magee, K. P., & Head, J. W. (1995). The role of rifting in the generation of melt: Implications for the origin and evolution of the Lada Terra-Lavinia Planitia region of Venus. *Journal of Geophysical Research*, *100*(E1), 1527–1552. https://doi.org/10.1029/94JE02334

Maia, J. S., & Wieczorek, M. A. (2022). Lithospheric structure of Venusian crustal plateaus. *Journal of Geophysical Research: Planets*, *127*(2), e2021JE007004. https://doi.org/10.1029/2021je007004

Manatschal, G., Lavier, L., & Chenin, P. (2015). The role of inheritance in structuring hyperextended rift systems: Some considerations based on observations and numerical modeling. *Gondwana Research*, *27*(1), 140–164. https://doi.org/10.1016/j.gr.2014.08.006

Marotta, A. M., Restelli, F., Bollino, A., Regorda, A., & Sabadini, R. (2020). The static and time-dependent signature of ocean-continent and ocean-ocean subduction: The case studies of Sumatra and Mariana complexes. *Geophysical Journal International*, *221*(2), 788–825. https://doi.org/10.1093/gji/ggaa029

Masursky, H., Eliason, E., Ford, P. G., McGill, G. E., Pettengill, G. H., Schaber, G. G., & Schubert, G. (1980). Pioneer Venus radar results: Geology from images and altimetry. *Journal of Geophysical Research*, *85*(A13), 8232–8260. https://doi.org/10.1029/JA085iA13p08232

McGill, G. E., Steenstrup, S. J., Barton, C., & Ford, P. G. (1981). Continental rifting and the origin of Beta Regio, Venus. *Geophysical Research Letters*, *8*(7), 737–740. https://doi.org/10.1029/GL008i007p00737

Moore, W. B., Simon, J. I., & Webb, A. A. G. (2017). Heat-pipe planets. *Earth and Planetary Science Letters*, *474*, 13–19. https://doi.org/10.1016/j.epsl.2017.06.015

Moresi, L., Dufour, F., & Mühlhaus, H. (2003). A Lagrangian integration point finite element method for large deformation modeling of visco-elastic geomaterials. *Journal of Computational Physics*, *184*(2), 476–497. https://doi.org/10.1016/S0021-9991(02)00031-1

Moresi, L., & Gurnis, M. (1996). Constraints on the lateral strength of slabs from three-dimensional dynamic flow models. *Earth and Planetary Science Letters*, *138*(1), 15–28. https://doi.org/10.1016/0012-821X(95)00221-W

Moresi, L., & Solomatov, V. (1998). Mantle convection with a brittle lithosphere: Thoughts on the global tectonic styles of the Earth and Venus. *Geophysical Journal International*, *133*(3), 669–682. https://doi.org/10.1046/j.1365-246x.1998.00521.x

Naliboff, J. B., & Buiter, S. J. H. (2015). Rift reactivation and migration during multiphase extension. *Earth and Planetary Science Letters*, *421*, 58–67. https://doi.org/10.1016/j.epsl.2015.03.050

Naliboff, J. B., Buiter, S. J. H., Peron-Pinvidic, G., Osmundsen, P. T., & Tetreault, J. L. (2017). Complex fault interaction controls continental rifting. *Nature Communications*, *8*(1179), 1179. https://doi.org/10.1038/s41467-017-00904-x

Neuharth, D., Brune, S., Wrona, T., Glerum, A., Braun, J., & Yuan, X. (2022). Evolution of rift systems and their fault networks in response to surface processes. *Tectonics*, *41*(3). https://doi.org/10.1029/2021TC007166

Nonn, C., Leroy, S., Lescanne, M., & Castilla, R. (2019). Central Gulf of Aden conjugate margins (Yemen-Somalia): Tectono-sedimentary and magmatism evolution in hybrid-type margins. *Marine and Petroleum Geology*, *105*, 100–123. https://doi.org/10.1016/j.marpetgeo.2018.11.053

Oliveira, M. E., Gomes, A. S., Rosas, F. M., Duarte, J. C., França, G. S., Almeida, J. C., & Fuck, R. A. (2022). Impact of crustal rheology and inherited mechanical weaknesses on early continental rifting and initial evolution of double graben structural configurations: Insights from 2D numerical models. *Tectonophysics*, *831*, 229281. https://doi.org/10.1016/j.tecto.2022.229281

O'Neill, C., Moresi, L., Müller, D., Albert, R., & Dufour, F. (2006). Ellipsis 3D: A particle-in-cell finite element hybrid code for modelling mantle convection and lithospheric deformation. *Computers & Geosciences*, *32*(10), 1769–1779. https://doi.org/10.1016/j.cageo.2006.04.006

O'Rourke, J. G., & Smrekar, S. E. (2018). Signatures of lithospheric flexure and elevated heat flow in stereo topography at coronae on Venus. *Journal of Geophysical Research: Planets*, *123*(2), 369–389. https://doi.org/10.1002/2017JE005358

Pauer, M., Fleming, K., & Čadek, O. (2006). Modeling the dynamic component of the geoid and topography of Venus. *Journal of Geophysical Research*, *111*(E11), E11012. https://doi.org/10.1029/2005JE002511

Pérez-Gussinyé, M., Andrés-Martínez, M., Araújo, M., Xin, Y., Armitage, J., & Morgan, J. P. (2020). Lithospheric strength and rift migration controls on synrift stratigraphy and breakup unconformities at rifted margins: Examples from numerical models, the Atlantic and South China Sea margins. *Tectonics*, *39*(12), e2020TC006255. https://doi.org/10.1029/2020TC006255

Peron-Pinvidic, G., Fourel, L., & Buiter, S. J. H. (2022). The influence of orogenic collision inheritance on rifted margin architecture: Insights from comparing numerical experiments to the mid-Norwegian margin. *Tectonophysics*, *828*, 229273. https://doi.org/10.1016/j.tecto.2022.229273

Petersen, K. D., Armitage, J. J., Nielsen, S. B., & Thybo, H. (2015). Mantle temperature as a control on the time scale of thermal evolution of extensional basins. *Earth and Planetary Science Letters*, *409*, 61–70. https://doi.org/10.1016/j.epsl.2014.10.043

Petersen, K. D., Schiffer, C., & Nagel, T. (2018). LIP formation and protracted lower mantle upwelling induced by rifting and delamination. *Scientific Reports*, *8*(16578), 2045–2322. https://doi.org/10.1038/s41598-018-34194-0

Popov, A. A., & Sobolev, S. V. (2008). SLIM3D: A tool for three-dimensional thermomechanical modeling of lithospheric deformation with elasto-visco-plastic rheology. *Physics of the Earth and Planetary Interiors*, *171*(1–4), 55–75. https://doi.org/10.1016/j.pepi.2008.03.007

Price, M., & Suppe, J. (1995). Constraints on the resurfacing history of Venus from the hypsometry and distribution of volcanism, tectonism, and impact craters. *Earth, Moon, and Planets*, *71*(1–2), 99–145. https://doi.org/10.1007/bf00612873

Püthe, C., & Gerya, T. (2014). Dependence of mid-ocean ridge morphology on spreading rate in numerical 3-D models. *Gondwana Research*, *25*(1), 270–283. https://doi.org/10.1016/j.gr.2013.04.005

Quinquis, M. E., & Buiter, S. J. (2014). Testing the effects of basic numerical implementations of water migration on models of subduction dynamics. *Solid Earth*, *5*(1), 537–555. https://doi.org/10.5194/se-5-537-2014

Regorda, A. (2022). Falcon for Venus. *Zenodo*. https://doi.org/10.5281/zenodo.7446601
Regorda, A., Spalla, M. I., Roda, M., Lardeaux, J.-M., & Marotta, A. M. (2021). Metamorphic facies and deformation fabrics diagnostic of subduction: Insights from 2D numerical models. *Geochemistry, Geophysics, Geosystems*, *22*(10), e2021GC009899. https://doi.org/10.1029/2021GC009899
Regorda, A., Thieulot, C., van Zelst, I., Zoltán, E., & Buiter, S. (2022). Venus rifting: Dataset vtu files. *Zenodo*. https://doi.org/10.5281/zenodo.7424003
Resor, P. G., Gilmore, M. S., Straley, B., Senske, D. A., & Herrick, R. R. (2021). Felsic tesserae on Venus permitted by lithospheric deformation models. *Journal of Geophysical Research: Planets*, *126*(4), e2020JE006642. https://doi.org/10.1029/2020JE006642
Richter, M. J. E. A., Brune, S., Riedl, S., Glerum, A., Neuharth, D., & Strecker, M. R. (2021). Controls on asymmetric rift dynamics: Numerical modeling of strain localization and fault evolution in the Kenya rift. *Tectonics*, *40*(5), e2020TC006553. https://doi.org/10.1029/2020TC006553
Rolf, T., Capitanio, F. A., & Tackley, P. J. (2018). Constraints on mantle viscosity structure from continental drift histories in spherical mantle convection models. *Tectonophysics*, *746*, 339–351. https://doi.org/10.1016/j.tecto.2017.04.031
Rolf, T., Steinberger, B., Sruthi, U., & Werner, S. C. (2018). Inferences on the mantle viscosity structure and the post-overturn evolutionary state of Venus. *Icarus*, *313*, 107–123. https://doi.org/10.1016/j.icarus.2018.05.014
Rolf, T., Weller, M., Gülcher, A., Byrne, P., O'Rourke, J. G., Herrick, R., et al. (2022). Dynamics and evolution of Venus' mantle through time. *Space Science Reviews*, *218*(70), 70. https://doi.org/10.1007/s11214-022-00937-9
Rutter, E., & Brodie, K. (2004). Experimental grain size-sensitive flow of hot-pressed Brazilian quartz aggregates. *Journal of Structural Geology*, *26*(11), 2011–2023. https://doi.org/10.1016/j.jsg.2004.04.006
Rybacki, E., Gottschalk, M., Wirth, R., & Dresen, G. (2006). Influence of water fugacity and activation volume on the flow properties of fine-grained anorthite aggregates. *Journal of Geophysical Research*, *111*(B3), B03203. https://doi.org/10.1029/2005JB003663
Sandwell, D. T., Johnson, C. L., Bilotti, F., & Suppe, J. (1997). Driving forces for limited tectonics on Venus. *Icarus*, *129*(1), 232–244. https://doi.org/10.1006/icar.1997.5721
Sandwell, D. T., & Schubert, G. (1992). Evidence for retrograde lithospheric subduction on Venus. *Science*, *257*(5071), 766–770. https://doi.org/10.1126/science.257.5071.766
Saunders, R. S., & Pettengill, G. H. (1991). Magellan: Mission summary. *Science*, *252*(5003), 247–249. https://doi.org/10.1126/science.252.5003.247
Schaber, G. G. (1982). Venus: Limited extension and volcanism along zones of lithospheric weakness. *Geophysical Research Letters*, *9*(5), 499–502. https://doi.org/10.1029/GL009i005p00499
Schmalholz, S. M. (2011). A simple analytical solution for slab detachment. *Earth and Planetary Science Letters*, *304*(1–2), 45–54. https://doi.org/10.1016/j.epsl.2011.01.011
Schmeling, H., Babeyko, A., Enns, A., Faccenna, C., Funiciello, F., Gerya, T., et al. (2008). A benchmark comparison of spontaneous subduction models—Towards a free surface. *Physics of the Earth and Planetary Interiors*, *171*(1–4), 198–223. https://doi.org/10.1016/j.pepi.2008.06.028
Schubert, G., & Sandwell, D. (1995). A global survey of possible subduction sites on Venus. *Icarus*, *117*(1), 173–196. https://doi.org/10.1006/icar.1995.1150
Schubert, G., Turcotte, D. L., & Olson, P. (2001). *Mantle convection in the Earth and planets*. Cambridge University Press. https://doi.org/10.1017/CBO9780511612879
Shalygin, E. V., Markiewicz, W. J., Basilevsky, A. T., Titov, D. V., Ignatiev, N. I., & Head, J. W. (2015). Active volcanism on Venus in the Ganiki Chasma rift zone. *Geophysical Research Letters*, *42*(12), 4762–4769. https://doi.org/10.1002/2015GL064088
Sharples, W., Moresi, L.-N., Jadamec, M. A., & Revote, J. (2015). Styles of rifting and fault spacing in numerical models of crustal extension. *Journal of Geophysical Research: Solid Earth*, *120*(6), 4379–4404. https://doi.org/10.1002/2014JB011813
Sim, S. J., Spiegelman, M., Stegman, D. R., & Wilson, C. (2020). The influence of spreading rate and permeability on melt focusing beneath mid-ocean ridges. *Physics of the Earth and Planetary Interiors*, *304*, 106486. https://doi.org/10.1016/j.pepi.2020.106486
Simons, M., Solomon, S. C., & Hager, B. H. (1997). Localization of gravity and topography: Constraints on the tectonics and mantle dynamics of Venus. *Geophysical Journal International*, *131*(1), 24–44. https://doi.org/10.1111/j.1365-246X.1997.tb00593.x
Sleep, N. H., & Warren, J. M. (2014). Effect of latent heat of freezing on crustal generation at low spreading rates. *Geochemistry, Geophysics, Geosystems*, *15*(8), 3161–3174. https://doi.org/10.1002/2014GC005423
Smrekar, S. E., Elkins-Tanton, L., Leitner, J. J., Lenardic, A., Mackwell, S., Moresi, L., et al. (2007). Tectonic and thermal evolution of Venus and the role of volatiles: Implications for understanding the terrestrial planets. In *Exploring Venus as a terrestrial planet* (pp. 45–71). American Geophysical Union (AGU). https://doi.org/10.1029/176GM05
Smrekar, S. E., Hensley, S., Dyar, M., Helbert, J., Andrews-Hanna, J., Breuer, D., et al. (2020). VERITAS (Venus Emissivity, Radio science, InSAR, Topography, and Spectroscopy): A proposed Discovery mission. In *European Planetary Science Congress* (p. EPSC2020-447).
Smrekar, S. E., Hoogenboom, T., Johnston, S., Stofan, E., Buck, R., & Martin, P. (2007). Major rifts on Venus: Lithospheric properties and formation of Parga and Hecate Chasmata. In *AGU Fall Meeting Abstracts*.
Smrekar, S. E., Ostberg, C., & O'Rourke, J. (2022). Venus variable lithosphere thickness and implications for active rifting and new insights on convective regime. In *LPSC abstract*.
Smrekar, S. E., Stofan, E. R., Mueller, N., Treiman, A., Elkins-Tanton, L., Helbert, J., et al. (2010). Recent hotspot volcanism on Venus from VIRTIS emissivity data. *Science*, *328*(5978), 605–608. https://doi.org/10.1126/science.1186785
Sobolev, S. V., & Babeyko, A. Y. (2005). What drives orogeny in the Andes? *Geology*, *33*(8), 617–620. https://doi.org/10.1130/G21557.1
Solomon, S. C. (1993). The geophysics of Venus. *Physics Today*, *46*(7), 48–55. https://doi.org/10.1063/1.881359
Solomon, S. C., & Head, J. (1984). Rift structures on Venus: Implications of a lithospheric stretching model. In *Lunar and Planetary Science Conference* (Vol. 15, pp. 806–807).
Solomon, S. C., & Head, J. (1985). Rift systems on Venus: An assessment of mechanical and thermal models. *Heat and detachment in crustal extension on continents and planets* (Vol. *575*, p. 138).
Solomon, S. C., Smrekar, S. E., Bindschadler, D. L., Grimm, R. E., Kaula, W. M., McGill, G. E., et al. (1992). Venus tectonics: An overview of Magellan observations. *Journal of Geophysical Research*, *97*(E8), 13199–13255. https://doi.org/10.1029/92JE01418
Spiegelman, M., May, D. A., Wilson, C. R., & Wilson, R. C. (2016). On the solvability of incompressible Stokes with viscoplastic rheologies in geodynamics. *Geochemistry, Geophysics, Geosystems*, *17*(6), 2213–2238. https://doi.org/10.1002/2015GC006228
Sternai, P. (2020). Surface processes forcing on extensional rock melting. *Scientific Reports*, *10*(1), 1–13. https://doi.org/10.1038/s41598-020-63920-w
Stoddard, P. R., & Jurdy, D. M. (2012). Topographic comparisons of uplift features on Venus and Earth: Implications for Venus tectonics. *Icarus*, *217*(2), 524–533. https://doi.org/10.1016/j.icarus.2011.09.003

Tavani, S., & Muñoz, J. A. (2012). Mesozoic rifting in the Basque–Cantabrian basin (Spain): Inherited faults, transversal structures and stress perturbation. *Terra Nova*, *24*(1), 70–76. https://doi.org/10.1111/j.1365-3121.2011.01040.x

Tetreault, J., & Buiter, S. J. (2018). The influence of extension rate and crustal rheology on the evolution of passive margins from rifting to break-up. *Tectonophysics*, *746*, 155–172. https://doi.org/10.1016/j.tecto.2017.08.029

Theunissen, T., & Huismans, R. S. (2019). Long-term coupling and feedback between tectonics and surface processes during non-volcanic rifted margin formation. *Journal of Geophysical Research: Solid Earth*, *124*(11), 12323–12347. https://doi.org/10.1029/2018JB017235

Theunissen, T., & Huismans, R. S. (2022). Mantle exhumation at magma-poor rifted margins controlled by frictional shear zones. *Nature Communications*, *13*(1), 1634. https://doi.org/10.1038/s41467-022-29058-1

Theunissen, T., Huismans, R. S., Lu, G., & Riel, N. (2022). Relative continent/mid-ocean ridge elevation: A reference case for isostasy in geodynamics. *Earth-Science Reviews*, *233*, 104153. https://doi.org/10.1016/j.earscirev.2022.104153

Thieulot, C. (2011). FANTOM: Two- and three-dimensional numerical modelling of creeping flows for the solution of geological problems. *Physics of the Earth and Planetary Interiors*, *188*(1–2), 47–68. https://doi.org/10.1016/j.pepi.2011.06.011

Thieulot, C. (2014). ELEFANT: A user-friendly multipurpose geodynamics code. *Solid Earth Discussions*, *6*(2), 1949–2096. https://doi.org/10.5194/sed-6-1949-2014

Thieulot, C., & Bangerth, W. (2022). On the choice of finite element for applications in geodynamics. *Solid Earth*, *13*(1), 229–249. https://doi.org/10.5194/se-13-229-2022

Thieulot, C., Fullsack, P., & Braun, J. (2008). Adaptive octree-based finite element analysis of two- and three-dimensional indentation problems. *Journal of Geophysical Research*, *113*(B12), B12207. https://doi.org/10.1029/2008JB005591

Tosi, N., Stein, C., Noack, L., Hüttig, C., Maierovà, P., Samuel, H., et al. (2015). A community benchmark for viscoplastic thermal convection in a 2-D square box. *Geochemistry, Geophysics, Geosystems*, *16*(7), 2175–2196. https://doi.org/10.1002/2015GC005807

Turcotte, D. L. (1993). An episodic hypothesis for Venusian tectonics. *Journal of Geophysical Research*, *98*(E9), 17061–17068. https://doi.org/10.1029/93JE01775

Uppalapati, S., Rolf, T., Crameri, F., & Werner, S. C. (2020). Dynamics of lithospheric overturns and implications for Venus's surface. *Journal of Geophysical Research: Planets*, *125*(11), e2019JE006258. https://doi.org/10.1029/2019JE006258

van den Broek, J., Magni, V., Gaina, C., & Buiter, S. (2020). The formation of continental fragments in subduction settings: The importance of structural inheritance and subduction system dynamics. *Journal of Geophysical Research: Solid Earth*, *125*(1), e2019JB018370. https://doi.org/10.1029/2019JB018370

Van Keken, P. E., King, S. D., Schmeling, H., Christensen, U. R., Neumeister, D., & Doin, M.-P. (1997). A comparison of methods for the modeling of thermochemical convection. *Journal of Geophysical Research*, *102*(B10), 22477–22495. https://doi.org/10.1029/97JB01353

van Zelst, I., Crameri, F., Pusok, A. E., Glerum, A., Dannberg, J., & Thieulot, C. (2022). 101 geodynamic modelling: How to design, interpret, and communicate numerical studies of the solid Earth. *Solid Earth*, *13*(3), 583–637. https://doi.org/10.5194/se-13-583-2022

Wang, H., Agrusta, R., & van Hunen, J. (2015). Advantages of a conservative velocity interpolation (CVI) scheme for particle-in-cell methods with application in geodynamic modeling. *Geochemistry, Geophysics, Geosystems*, *16*(6), 2015–2023. https://doi.org/10.1002/2015GC005824

Wang, Z., Kusky, T. M., & Capitanio, F. A. (2016). Lithosphere thinning induced by slab penetration into a hydrous mantle transition zone. *Geophysical Research Letters*, *43*(22), 11567–11577. https://doi.org/10.1002/2016GL071186

Warren, C. J., Beaumont, C., & Jamieson, R. A. (2008a). Deep subduction and rapid exhumation: Role of crustal strength and strain weakening in continental subduction and ultrahigh-pressure rock exhumation. *Tectonics*, *27*(6), 1–28. https://doi.org/10.1029/2008TC002292

Warren, C. J., Beaumont, C., & Jamieson, R. A. (2008b). Modelling tectonic styles and ultra-high pressure (UHP) rock exhumation during the transition from oceanic subduction to continental collision. *Earth and Planetary Science Letters*, *267*(1–2), 129–145. https://doi.org/10.1016/j.epsl.2007.11.025

Wenker, S., & Beaumont, C. (2018). Effects of lateral strength contrasts and inherited heterogeneities on necking and rifting of continents. *Tectonophysics*, *746*, 46–63. https://doi.org/10.1016/j.tecto.2016.10.011

Wessel, P., & Smith, W. H. F. (1998). New, improved version of generic mapping tools released. *Eos, Transactions American Geophysical Union*, *79*(47), 579–579. https://doi.org/10.1029/98EO00426

Wessel, P., & Smith, W. M. F. (2001). New improved version of generic mapping tools released. *EOS Transactions of the American Geophysical Union*, *79*(47), 579. https://doi.org/10.1029/98eo00426

Wilson, C. F., Widemann, T., & Ghail, R. (2021). Venus: Key to understanding the evolution of terrestrial planets. *Experimental Astronomy*. https://doi.org/10.1007/s10686-021-09766-0

Xiao, C., Li, F., Yan, J.-G., Hao, W.-F., Harada, Y., Ye, M., & Barriot, J. P. (2020). Inversion of Venus internal structure based on geodetic data. *Research in Astronomy and Astrophysics*, *20*(8), 127. https://doi.org/10.1088/1674--4527/20/8/127

Youssef, S. E.-H. (2015). Seismicity and seismotectonic setting of the Red Sea and adjacent areas. In N. M. Rasul & I. C. Stewart (Eds.), *The Red Sea: The formation, morphology, oceanography and environment of a young ocean basin* (pp. 151–159). Springer Berlin Heidelberg. https://doi.org/10.1007/978-3-662-45201-1_8

Zalesak, S. T. (1979). Fully multidimensional flux-corrected transport algorithms for fluids. *Journal of Computational Physics*, *31*(3), 335–362. https://doi.org/10.1016/0021-9991(79)90051-2

Zhong, S., Zuber, M. T., Moresi, L., & Gurnis, M. (2000). Role of temperature-dependent viscosity and surface plates in spherical shell models of mantle convection. *Journal of Geophysical Research*, *105*(B5), 11063–11082. https://doi.org/10.1029/2000JB900003

Zuber, M., & Parmentier, E. (1986). Lithospheric necking: A dynamic model for rift morphology. *Earth and Planetary Science Letters*, *77*(3), 373–383. https://doi.org/10.1016/0012-821X(86)90147-0

Zwaan, F., Corti, G., Sani, F., Keir, D., Muluneh, A. A., Illsley-Kemp, F., & Papini, M. (2020). Structural analysis of the Western Afar Margin, East Africa: Evidence for multiphase rotational rifting. *Tectonics*, *39*(7), 1–25. https://doi.org/10.1029/2019TC006043

Zwaan, F., Schreurs, G., Naliboff, J., & Buiter, S. J. (2016). Insights into the effects of oblique extension on continental rift interaction from 3D analogue and numerical models. *Tectonophysics*, *693*, 239–260. https://doi.org/10.1016/j.tecto.2016.02.036